

Higgs, top and electro-weak precision measurements at future e^+e^- colliders; a combined effective field theory analysis with renormalization mixing

Sunghoon Jung,^a Junghwan Lee,^a Martin Perelló,^b Junping Tian,^c Marcel Vos^b

^a*CTP, Department of Physics and Astronomy, Seoul National University, Seoul 08826, Korea*

^b*IFIC, Universitat de València and CSIC, c./ Catedrático José Beltrán 2, E-46980 Paterna, Spain*

^c*ICEPP, The University of Tokyo, Hongo, Bunkyo-ku, Tokyo, 113-0033, Japan*

E-mail: sunghoonj@snu.ac.kr, ghe1266@snu.ac.kr,
martin.perello@ific.uv.es, tian@icepp.s.u-tokyo.ac.jp,
marcel.vos@cern.ch

ABSTRACT: This paper presents a combined analysis of the potential of a future electron-positron collider to constrain the Higgs, top and electro-weak (EW) sectors of the Standard Model Effective Field Theory (SMEFT). The leading contributions of operators involving top quarks arise mostly at one-loop suppressed order and can be captured by the renormalization group mixing with Higgs operators. We perform global fits with an extended basis of 29 parameters, including both Higgs and top operators, to the projections for the Higgs, top and electro-weak precision measurements at the International Linear Collider (ILC). The determination of the Higgs boson couplings in the 250 GeV stage of the ILC is initially severely degraded by the additional top-quark degrees of freedom, but can be nearly completely recovered by the inclusion of precise measurements of top-quark EW couplings at the LHC. The physical Higgs couplings are relatively robust, as the top mass is larger than the energy scale of EW processes. The effect of the top operators on the bounds on the Wilson coefficients is much more pronounced and may limit our ability to identify the source of deviations from the Standard Model. Robust global bounds on all Wilson coefficients are only obtained when the 500 GeV stage of the ILC is included.

Contents

1	Introduction	1
2	Motivation and background	3
2.1	Top-Higgs interplay in the SM	3
2.2	BSM motivation	4
3	Theoretical framework	5
3.1	Higgs/EW operators	5
3.2	Top operators	7
3.3	Top Yukawa coupling	7
3.4	Power counting for top-loop contributions	8
3.5	Renormalization group evolution and scale choice	10
3.6	Finite one-loop effects of top couplings	13
3.7	Summary	14
4	Benchmark datasets	15
4.1	LEP/SLC electro-weak precision observables	15
4.2	Selected LHC Higgs measurements	16
4.3	LHC top production - run 2	16
4.4	HL-LHC top production - S2 scenario	16
4.5	ILC Higgs/EW measurements at $\sqrt{s} = 250$ GeV	17
4.6	ILC Higgs/EW measurements at $\sqrt{s} = 500$ GeV	17
4.7	ILC top quark pair production at $\sqrt{s} = 500$ GeV	17
5	Global-fit analysis	17
5.1	Method	17
5.2	Results for the ILC at $\sqrt{s} = 250$ GeV	18
5.3	The role of beam polarization	21
5.4	The role of electro-weak measurements	23
5.5	Results for higher-energy operation – ILC 500 stage	25
5.6	The Higgs self-coupling	27
5.7	Indirect bounds on top-EW couplings	28
5.8	The top-quark Yukawa coupling	30
6	Summary	31

A	Typos and corrections in Ref.[1]	34
B	Comparison with Ref.[2, 3]	38
	B.1 Operator choice	38
	B.2 Finite versus log effects of top quarks	39
	B.3 Higher-order effects of top quarks	41
C	Results with different renormalization scale Q	44
D	The Q_0 scale dependence	47
	D.1 The running of the covariance matrix	47
	D.2 The Q_0 independence of the uncertainty of observables	48
	D.3 The interpretation of the Q_0 dependence - Oblique parameters	49
E	RG evolution with bottom operators and their impact	51
F	Observables in terms of operators	52
G	Numerical results	57
H	Covariance matrices	59

1 Introduction

With the discovery of the Higgs boson, all particles postulated by the Standard Model (SM) of particle physics have been experimentally confirmed. Many attempts have been made to embed the SM in a more complete theory, that incorporates a description of gravity, neutrino masses, or dark matter, to name a few of the most popular targets. Currently, none of these extensions have imposed themselves as the “standard” paradigm.

In the meantime, experiments are leaving no stones unturned looking for hints of new physics. The LHC provides precise measurements of a wealth of SM processes in an unexplored energy regime. Future colliders may extend the energy reach and precision still further. We focus on an electron-positron collider with sufficient energy to produce Higgs bosons and eventually top quarks, and adopt in particular the scenario¹ of the ILC [8, 9].

¹A “Higgs factory” can also be implemented as a linear collider based on *warm* radio-frequency technology (CLIC [4, 5]) or a 100 km ring (FCCee [6], CEPC [7]).

Effective-field theory (EFT) or the Standard Model EFT (SMEFT) is a crucial tool in modern high-energy physics, as it provides a relatively model-independent framework to order and interpret the enormous wealth of measurements from experiments at colliders and elsewhere. This approach is particularly needed when one is to extract some properties in a model-independent way. Some of the earliest works along this direction have focused on LHC Higgs physics [10–12] and top physics [13–17]². EFT studies also provide a global framework to compare scenarios for future colliders in terms of the sensitivity of their precision measurements to new physics. We build on studies for future collider prospects that have been performed in the Higgs/EW [1, 19] and top sector [15, 20].

In this study, we combine the contributions from the Higgs/EW and top sectors that have been treated separately so far. The top-sector contributions to Higgs+EW precision observables have been ignored as they are one-loop suppressed compared to those of Higgs operators and SM. However, these are leading contributions of the top sector at the initial stages of ILC at 250 GeV, before top quarks can be directly produced.

Therefore, it is important to include top contributions and assess whether the Higgs precision achievable without model-independent top effects can be retained even with them, what capabilities of future colliders are needed, and whether the top sector can be precisely constrained without direct top productions.

To this end, we extend the previous SMEFT basis of Ref. [1, 19] to include seven additional operators involving top quarks. We thus include a total of 29 degrees of freedom that affect Higgs production and decay rates, EW precision measurements and high-energy di-boson production, and the EW interactions of the top quark. We include all and only leading contributions of these operators, up to *log-enhanced* one-loop contributions compared to the SM ones, as captured by Higgs and top operator mixing through the renormalization group (RG) evolution of Higgs operators due to top operators³.

We first treat the additional top operators as a *threat* to the Higgs fit and evaluate how the extension of the operator basis with top-quark operators affects the determination of the Higgs boson couplings. We investigate how precise measurements of top quark electro-weak couplings at the LHC or future measurements at the ILC at $\sqrt{s} = 500$ GeV can mitigate this effect. We also consider the new *opportunity* that the interplay between top and Higgs physics offers. We discuss to what extent the

²Recently, differential distributions of EW processes have also been included in SMEFT analyses [18].

³The authors of Ref. [2, 3] have developed a similar approach and used it to study the prospects of circular electron-positron colliders. Their studies are compared with ours in [Appendix B](#).

250 GeV “Higgs factory” programme can do top physics without actually producing top quarks by using Higgs/EW precision measurements to set indirect bounds on the top operator coefficients.

The paper is structured as follows. In Section 2 and Section 3 we present the motivation and the theory framework, with details of the operator basis, power counting of top effects, and renormalization group effects. Section 4 presents the benchmark datasets that are used in the fit. The main results are presented in Section 5. In Section 6, we summarize the most important findings of the study and discuss their implications.

2 Motivation and background

The top-sector’s contributions to the Higgs+EW observables are the leading top contributions to the initial “Higgs factory” stage of future electron-positron colliders. There are various good reasons to expect that top-sector contributions can be important, numerically.

2.1 Top-Higgs interplay in the SM

In practice, we expect the most important next-to-lowest effects would come from loop effects induced by top-quark related operators. It is first because the top-EW interactions are only poorly constrained by the LHC and the initial (250 GeV) stage of future Higgs factories does not reach the top quark pair production threshold.

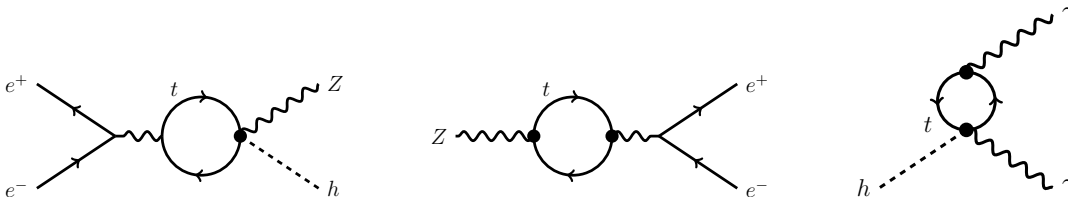


Figure 1. Example loop diagrams involving top quarks in $e^+e^- \rightarrow Zh$ production (left), $Z \rightarrow e^+e^-$ (middle) and $h \rightarrow \gamma\gamma$ (right). The solid black dots indicate vertices that are affected by the operators considered in this paper.

Figure 1 shows three example loop processes where top-EW couplings can contribute. The contribution of top-loop diagrams involving poorly constrained operators can easily exceed the experimental accuracies of the rate measurements for those processes. The first diagram contributes directly to the dominant Higgs production process,

and would hence affect the Higgs coupling measurements. The second diagram contributes to the Z -pole process and will play a role in electro-weak precision observables⁴ (EWPO). The third diagram contributes to the $h \rightarrow \gamma\gamma$ branching ratio.

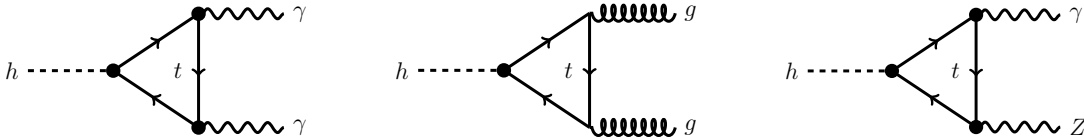


Figure 2. Loop diagrams for Higgs boson interactions with photons (left), gluons (middle), and with a photon and Z -boson (right). The solid black dots indicate vertices that are affected by the operators considered in this paper.

Another reason is that the top quark couples to the SM most strongly. This makes the top-loop the dominant contribution to the loop-induced Higgs decays and productions in the SM, as shown in Fig. 2. In a calculation that explicitly resolves the loop diagrams, the three diagrams depend on various top-EW couplings, including the $t\bar{t}h$, $t\bar{t}\gamma$, $t\bar{t}g$, and $t\bar{t}Z$ vertices⁵. Also, such vertex contributions are *not* loop suppressed compared to those of SM ones. Therefore, Higgs precision measurements can be sensitive to new physics that affect the top-EW vertices. Higgs factories operating at $\sqrt{s} = 250$ GeV can probe these vertices indirectly. The inclusion of these loop effects is described in Section 3.6 and a quantitative analysis is presented in Section 5.8 and Section 5.7.

2.2 BSM motivation

A further entanglement of the Higgs and top sectors may arise in new physics models beyond the SM (BSM). Generally speaking, extensions of the Standard Model are under no obligation to respect the separation between the top and Higgs sectors. Rather, concrete extensions of the SM do activate multiple operators across several sectors.

A well-known example is found in composite Higgs models [23, 24]. The Higgs boson couplings are expected to deviate from the SM predictions as $\kappa \sim 1 - c \times \frac{1 \text{ TeV}}{f}$,

⁴For an analogy, consider the W -mass measurement. The SM computation of m_W receives an uncertainty from top mass uncertainty ($\Delta m_W \sim 6$ MeV for $\Delta m_t \sim 1$ GeV [21]). At a certain precision of m_W , further improvements of the experimental measurement will not increase the precision of the comparison, unless one can improve the top-quark mass measurement as well.

⁵Indeed, in the so-called *resolved* version of the fit in κ framework used for early LHC analyses [10] the scale factors for the effective Higgs boson coupling to gluons are written as $\kappa_g \sim \kappa_t + \Delta\kappa_g$ and that to photons as $\kappa_\gamma \sim -0.28\kappa_t + 1.28\kappa_W + \Delta\kappa_\gamma$ [22], where κ_t and κ_W are the scale factors that multiply the SM predictions for the Higgs boson couplings to the top quark and the W -boson ($\kappa_g = \kappa_\gamma = \kappa_t = \kappa_W = 1$ and $\Delta\kappa_g = \Delta\kappa_\gamma = 0$ in the SM).

where f is the scale associated with the new physics and $c \sim 3\%$ for vector boson couplings and $c \sim 3 - 9\%$ for fermion couplings [22]. As the top quark is the heaviest SM particle and consequently tends to mix strongly with the composite sector, the top-EW couplings are typically altered sizably. A custodial symmetry is usually invoked to protect the coupling of the Z -boson to left-handed bottom quarks, but cannot simultaneously avoid large corrections to the EW couplings of the top quark [25, 26]. Ref. [27] indeed collects a number of concrete proposals for composite Higgs models that predict sizeable (up to 10-20%) deviations from the SM for the top quark couplings to the Z -boson. Ref. [28] quantitatively demonstrated that the measurements of Higgs boson and top (and bottom) quark couplings provide complementary handles. Together, precise measurements of the top, Higgs and EW sectors probe the parameter space of typical models up to a scale well beyond the direct reach of colliders. A comprehensive study of the constraints of precision measurements on such models requires a combined analyses of Higgs and top measurements.

3 Theoretical framework

In this section, we present the extended basis of dimension-six operators, including the Higgs operators proposed in Ref. [1] and additional top operators. Then we detail various top-quark effects that we include, with the power counting rules to select which top effects to include with the renormalization group calculation.

3.1 Higgs/EW operators

Following [1], we use the 10 ‘Higgs’ operators below to parameterize the lowest-order modifications of Higgs and EW observables.

$$\begin{aligned}
\mathcal{O}_H &= \partial^\mu(\Phi^\dagger\Phi)\partial_\mu(\Phi^\dagger\Phi), & \mathcal{O}_T &= (\Phi^\dagger\overleftrightarrow{D}^\mu\Phi)(\Phi^\dagger\overleftrightarrow{D}_\mu\Phi), \\
\mathcal{O}_6 &= (\Phi^\dagger\Phi)^3, & \mathcal{O}_{WB} &= \Phi^\dagger t^a \Phi W_{\mu\nu}^a B^{\mu\nu}, \\
\mathcal{O}_{BB} &= \Phi^\dagger\Phi B_{\mu\nu}B^{\mu\nu}, & \mathcal{O}_{3W} &= \epsilon_{abc}W_{\mu\nu}^a W_{\rho}^{b\nu}W^{c\rho\mu}, \\
\mathcal{O}_{HL} &= (\Phi^\dagger i\overleftrightarrow{D}^\mu\Phi)(\bar{L}\gamma_\mu L), & \mathcal{O}_{HL'} &= (\Phi^\dagger t^a i\overleftrightarrow{D}^\mu\Phi)(\bar{L}\gamma_\mu t^a L), \\
\mathcal{O}_{HE} &= (\Phi^\dagger i\overleftrightarrow{D}^\mu\Phi)(\bar{e}\gamma_\mu e), & \mathcal{O}_{WW} &= (\Phi^\dagger\Phi)W_{\mu\nu}^a W^{a\mu\nu},
\end{aligned} \tag{3.1}$$

with the Lagrangian terms

$$\begin{aligned}
\Delta\mathcal{L}_{\text{Higgs}} &= \frac{c_H}{2v^2}\mathcal{O}_H + \frac{c_T}{2v^2}\mathcal{O}_T - \frac{c_6\lambda}{v^2}\mathcal{O}_6 + \frac{g^2c_{WW}}{m_W^2}\mathcal{O}_{WW} + \frac{4gg'c_{WB}}{m_W^2}\mathcal{O}_{WB} + \frac{g'^2c_{BB}}{m_W^2}\mathcal{O}_{BB} \\
&+ \frac{g^3c_{3W}}{m_W^2}\mathcal{O}_{3W} + \frac{c_{HL}}{v^2}\mathcal{O}_{HL} + \frac{4c'_{HL}}{v^2}\mathcal{O}_{HL'} + \frac{c_{HE}}{v^2}\mathcal{O}_{HE},
\end{aligned} \tag{3.2}$$

where the Higgs vacuum expectation value $v = 246$ GeV and $t^a = \frac{1}{2}\tau^a$ (τ^a are Pauli matrices). We do not assume oblique [29, 30] or universal [31] corrections and treat all ten operators as independent. We also add Yukawa operators $c_{bH, cH, \tau H, \mu H}$, to the SM fermions (e.g. $\mathcal{O}_{bH} = (\Phi^\dagger \Phi)(\bar{Q}b\Phi)$) and the collective gluonic operators c_{gH} and $\mathcal{C}_{W,Z}$ to effectively describe the Higgs decay widths and corresponding physical Higgs couplings. We refer to Ref. [1] for a detailed discussion of this operator set.

We denote $\delta A = \Delta A/A$ as the deviation of the observable A from its SM prediction. We express δA in terms of EFT coefficients. We also define the deviation of the *physical* Higgs coupling as the deviation of the square-root of the partial width [1, 32]

$$\delta g(hXX) \equiv \frac{1}{2}\delta\Gamma(h \rightarrow XX), \quad (3.3)$$

where X can be any particles to which the Higgs boson decays. For example,

$$\delta g(hb\bar{b}) = \frac{1}{2}\delta\Gamma(h \rightarrow b\bar{b}) = \frac{1}{2}(2c_{bH} - 2\delta v + \delta Z_h + \delta m_h), \quad (3.4)$$

where we explicitly write the dependence on δm_h and δv , and $\delta Z_h = -c_H$ is the correction to the Higgs field strength. This expression is slightly different from that of Ref. [1] where c_{bH} was used to collectively describe c_{bH} , δv and δm_h altogether. They are separated to emphasize the dependence on the three parameters, but numerical results remain almost unchanged. We use a similar treatment for $\delta g(h\mu^+\mu^-)$, $\delta g(h\tau^+\tau^-)$, $\delta g(hc\bar{c})$.

The Higgs self-coupling is represented by $\bar{\lambda}$ defined as

$$\bar{\lambda} = \lambda \left(1 + \frac{3}{2}c_6 \right), \quad (3.5)$$

which is a combination of the original Higgs self-coupling λ and the operator c_6 shifting the Higgs potential. In the Higgs fit at $\sqrt{s} = 250$ GeV, $\bar{\lambda}$ is constrained by the Higgs mass measurement. Only this combination appears in our global fit until the di-Higgs production $e^+e^- \rightarrow Zh h$ is available at $\sqrt{s} = 500$ GeV. Although the Higgs pair production at HL-LHC can provide some handle, the ILC $\sigma(Zhh)$ measurement will eventually provide the most precise and robust determination of c_6 independently from λ [33]. Instead, for the early stage of the ILC at $\sqrt{s} = 250$ GeV, it is assumed that the HL-LHC data constrain c_6 well enough, so as not to affect the model-independent fit of other parameters [2]. It was also proposed to use the finite one-loop corrections of c_6 to the Higgsstrahlung process $e^+e^- \rightarrow Zh$ at ILC250 [34, 35] to constrain c_6 . This contribution is not considered in the power counting we adopt (more on this in Section 3.4). A more dedicated study could be interesting.

3.2 Top operators

To properly account for the dependence of Higgs precision observables on vertices involving top quarks, we include the following seven ‘top’ operators in our basis.

$$\begin{aligned}
\mathcal{O}_{tH} &= (\Phi^\dagger \Phi)(\bar{Q}t\tilde{\Phi}), & \mathcal{O}_{Hq}^{(1)} &= (\Phi^\dagger i \overleftrightarrow{D}_\mu \Phi)(\bar{Q}\gamma^\mu Q), \\
\mathcal{O}_{Hq}^{(3)} &= (\Phi^\dagger i \overleftrightarrow{D}_\mu^a \Phi)(\bar{Q}\gamma^\mu \tau^a Q), & \mathcal{O}_{Ht} &= (\Phi^\dagger i \overleftrightarrow{D}_\mu \Phi)(\bar{t}\gamma^\mu t), \\
\mathcal{O}_{Htb} &= (\tilde{\Phi}^\dagger i D_\mu \Phi)(\bar{t}\gamma^\mu b), \\
\mathcal{O}_{tW} &= (\bar{Q}\sigma^{\mu\nu}t)\tau^a \tilde{\Phi} W_{\mu\nu}^a, & \mathcal{O}_{tB} &= (\bar{Q}\sigma^{\mu\nu}t)\tilde{\Phi} B_{\mu\nu},
\end{aligned} \tag{3.6}$$

with

$$\Delta\mathcal{L}_{\text{top}} = -y_t \frac{c_{tH}}{v^2} \mathcal{O}_{tH} + \frac{c_{Hq}^{(1)}}{v^2} \mathcal{O}_{Hq}^{(1)} + \frac{c_{Hq}^{(3)}}{v^2} \mathcal{O}_{Hq}^{(3)} + \frac{c_{Ht}}{v^2} \mathcal{O}_{Ht} + \frac{c_{Htb}}{v^2} \mathcal{O}_{Htb} + \frac{c_{tW}}{v^2} \mathcal{O}_{tW} + \frac{c_{tB}}{v^2} \mathcal{O}_{tB}, \tag{3.7}$$

where Q is the third-generation left-handed quark doublet and $\tilde{\Phi} = i\tau_2\Phi^\dagger$. These are the top operators that affect Higgs and EW observables at one loop. We do not consider four-fermion operators that involve two top quarks. In this work, we calculate these one-loop effects using the Renormalization Group (RG) evolution and mixing of top and Higgs operators. Our power counting rule is discussed in Section 3.4, top RG effects in Section 3.5, and top effects that are not captured in this way in Section 3.6.

In several extensions of the Standard Model, the effect of the top operators may be accompanied by bottom-quark effects. We have evaluated the one-loop effects on the global fit and find them to be negligible. This is discussed in detail in [Appendix E](#).

3.3 Top Yukawa coupling

The operator coefficient c_{tH} shifts the top Yukawa coupling and the top mass at tree level. Including also Higgs operator contributions, we can write the following expression:

$$\Delta\mathcal{L} = -\frac{y_t v}{\sqrt{2}}(1 + \frac{1}{2}c_{tH})\bar{t}t - \frac{y_t}{\sqrt{2}}(1 + \frac{3}{2}c_{tH} + \frac{1}{2}\delta Z_h)h\bar{t}t \tag{3.8}$$

$$= -m_t\bar{t}t - \frac{m_t}{v}(1 + c_{tH} - \frac{1}{2}c_H)h\bar{t}t. \tag{3.9}$$

In the second line, we define the top mass as $m_t = y_t v / \sqrt{2}(1 + \frac{1}{2}c_{tH})$ and rewrite the Yukawa coupling in terms of the redefined top mass. Thus, we define the deviation of the top-quark Yukawa coupling as

$$\delta y_t \equiv c_{tH} - \frac{1}{2}c_H - \delta v. \tag{3.10}$$

The top-quark Yukawa coupling and its tree-level modification can be measured separately from the top mass and the $t\bar{t}h$ cross-section. The latter is available at the LHC and HL-LHC prospects will be used throughout in this work. The ILC can measure the top-quark Yukawa coupling directly at $\sqrt{s} = 500$ GeV stage (or, even better, 550 GeV [36]). The top-quark Yukawa coupling also affects Higgs decays $h \rightarrow \gamma\gamma, Z\gamma, gg$ via one-loop diagrams, which are available already at the low-energy running of ILC [37]. These are finite one-loop effects, but are important because SM contributions are also at one-loop. They are indeed included in our work consistently with the power-counting rule in Section 3.4 and further discussed in Section 3.6.

The coefficient c_{tH} appears in our global fits only through the top Yukawa coupling as in Eq. (3.10). It does not RG mix with any Higgs operators. The only exception is c_6 (as shown in Eq. (E.4)), but c_{tH} 's RG contributions cannot be measured in our global fits since c_6 appears only at one energy scale (i.e. from the Zhh production cross section at $\sqrt{s} = 500$ GeV). Thus, we do not include the RG evolution of c_6 .

3.4 Power counting for top-loop contributions

In this work, we consider a subset of the leading effects of top operators on precision measurements of Higgs and EW sectors. Although it is best to include the full leading effects, most of them are loop contributions, and hence not easy to calculate and understand. As a first step toward a complete study, it is better to focus on a consistent subset of important effects. This subsection develops a power counting to select such a subset.

One could hope to include all top contributions at a given *absolute order*. The one-loop corrections then unambiguously specify the top contributions from one-loop diagrams. But the fact that not all leading SM processes are generated at the same absolute order makes the issue complicated. Consider the Higgs decays $h \rightarrow \gamma\gamma, Z\gamma, gg$ versus the other Higgs processes. In the SM, the former are generated at one-loop while the latter are already present at tree-level. In a numerical analysis, we do include all those processes and treat them equally even though their absolute orders are different. It is because they are *leading* contributions to each observable. The underlying logic is that if measurement uncertainties of tree- and loop-induced observables are similar, those leading contributions will receive similar constraints, regardless of their absolute orders. Thus, they will be similarly important. The leading contribution has an important role, irrespective of its absolute order; it provides a new information for the first time, while subleading corrections usually only modify the leading information.

The same issue applies to top contributions to Higgs physics observables. Although we will be interested in leading top contributions regardless of their absolute orders, not all leading contributions are equally important. If the leading top contribution

arises at five-loop level, while the SM process is at tree-level, it is very unlikely that such leading top contribution have an impact, unless the observable is measured with exquisite precision. Here comes the notion of the *relative orders* of top contributions compared to the SM.

In all, **our rule is to include all and only leading top contributions up to the logarithmic one-loop order relative to the SM.** Most leading top effects arise at the one-loop order compared to the SM. Among the full one-loop corrections to SM processes, our rule is to include only logarithmic ones, which can be readily obtained through the RG evolution of Higgs operators induced by top operators. In other words, we include leading top effects up to the logarithmic one-loop compared to the SM. Whenever some Higgs operator contributes to some Higgs observables, its RG mixing with top operators accounts for those top operators' logarithmic one-loop corrections to the observables. This is our main method to include the leading top-loop effects in this work.

The logarithmic corrections are not full one-loop effects, but they are a convenient and self-consistent subset. The RG effects respect all the symmetries of the theory, including gauge invariance, so that most non-zero effects in the full one-loop corrections also arise in RG⁶. Due to the logarithm of scale ratios (e.g. Eq. (3.12)), the RG contributions are often the dominant contribution among full one-loop effects, although this is not always the case.

This approach is convenient because the RG evolution is much easier to calculate. It needs to be calculated only once for all operators, independently of the observables, while every new full one-loop effects must be calculated separately (the majority has been done [2, 3, 38]). Moreover, their contribution is easier to understand, e.g. based on operator mixing patterns [39, 40]. Thus, although full one-loop analysis will have to be eventually done (see, e.g. [2]), at this early stage we use RG effects as a convenient proxy for the leading top effects.

The power counting rule we propose is particularly useful if all observables are measured with similar errors. All leading contributions will receive similar constraints, regardless of their absolute orders. But if some observables are measured better, this logic may become biased. There is no obvious mathematical answer for which top contributions at which order must be included. At least, the RG parts are theoretically consistent and practically convenient proxies of leading loop effects.

There is a notable exception and subtlety with this power counting rule. It arises again from the fact that not all top contributions are at the same absolute and relative

⁶Some external momentum dependences of full one-loop effects are not captured by RG calculations. Such dependences can induce useful information on differential and energy-dependent observables.

	Higgs loop production/decay	other observables	top production
SM	finite 1-loop	tree-level	tree-level
Higgs operator	tree-level from $c_{WW,WB,BB}$ finite 1-loop from other operators	tree-level	none
top operator	log 1-loop via $\dot{c}_{WW,WB,BB}$ log 2-loop via other \dot{c} finite 1-loop via tree-shift of y_t, g_{Zt}	log 1-loop via \dot{c}	tree-level

Table 1. Summary of the *absolute* orders of the contributions that we include. Our power counting is discussed in Section 3.4; the RG-induced logarithmic loop effects of top operators in Section 3.5; the finite one-loop effects of top operators in loop-induced Higgs decays in Section 3.6. The treatment of top observables are from Ref. [15], where Higgs loop effects are neglected.

orders. Although SM $h \rightarrow \gamma\gamma, Z\gamma$ are induced at one-loop, $c_{WW,WB,BB}$ contribute at the (absolute) tree-level. Then, according to the power counting rule, two-loop RG evolutions of $c_{WW,WB,BB}$ and finite one-loop corrections are needed. But we include only one-loop RG evolutions of $c_{WW,WB,BB}$. This may leave some numerical uncertainties.

Some top effects are not captured by the renormalization of Higgs operators. As discussed in Section 3.3 and Section 3.6, there are tree-level shifts of SM parameters due to top operators: c_{tH} shifts the top Yukawa, and $c_{Hq}^{(1)}, c_{Hq}^{(3)}, c_{Ht}$ shift the $Zt\bar{t}$ coupling at the tree-level. We include such relative tree-level effects.

The power counting and the corrections that we include are summarized in Table 1. We also assess the numerical impact of our power counting rules in Appendices. First, the top contributions treated differently in our approach and in [2, 3] are compared in Appendix B; second, the uncertainties in our global fit introduced by the choice of RG scale Q (see next subsection) are estimated in Appendix C. We can conclude that the differences between different approaches are mostly within $\mathcal{O}(10)\%$ and our results are stable with respect to the variation of Q .

3.5 Renormalization group evolution and scale choice

The logarithmic one-loop contributions of top operators to Higgs/EW observables are captured by Higgs and top operator mixing, through the RG evolution of Higgs operators due to top operators. The RG equations of Higgs operators have the following form:

$$\dot{c}_i \equiv 16\pi^2 \frac{dc_i}{d\ln\mu} = \gamma_{ij} c_j, \quad (3.11)$$

where i index represents Higgs operators and j top operators. We do not consider Higgs self running between Higgs operators, as they are subleading corrections, while the RG mixing with top operators are leading top contributions to Higgs+EWPO observables. Likewise, we do not consider RG evolutions of top operators, as discussed in the previous subsections. An approximate solution to the RG equations is given by:

$$c_i(Q) \simeq c_i(Q_0) + \frac{1}{16\pi^2} \gamma_{ij} c_j(Q_0) \ln \frac{Q}{Q_0}. \quad (3.12)$$

The RG equations of the Higgs operators and γ_{ij} are given by [39, 41–43]: (in the MS-bar subtraction scheme with dimensional regularization)

$$\dot{c}_H = (12y_t^2 N_c - 4g^2 N_c) c_{Hq}^{(3)} - 12y_t y_b N_c c_{Htb}, \quad (3.13)$$

$$\dot{c}_T = (4y_t^2 N_c - \frac{8}{3} g'^2 Y_h Y_u N_c) c_{Ht} - (4y_t^2 N_c + \frac{8}{3} g'^2 Y_h Y_q N_c) c_{Hq}^{(1)} + 4y_t y_b N_c c_{Htb} \quad (3.14)$$

$$\dot{c}_{WW} = \frac{1}{4} (-2gy_t N_c c_{tW}), \quad (3.15)$$

$$\dot{c}_{BB} = \frac{1}{4t_W^2} (-4g' y_t (Y_q + Y_u) N_c c_{tB}), \quad (3.16)$$

$$\dot{c}_{WB} = \frac{1}{8t_W} (2gy_t N_c c_{tB} + 4g' y_t (Y_q + Y_u) N_c c_{tW}), \quad (3.17)$$

$$\dot{c}_{HL} = \frac{1}{2} Y_l g'^2 \left(\frac{16}{3} Y_q N_c c_{Hq}^{(1)} + \frac{8}{3} Y_u N_c c_{Ht} \right), \quad (3.18)$$

$$\dot{c}'_{HL} = \frac{2}{3} g^2 N_c c_{Hq}^{(3)}, \quad (3.19)$$

$$\dot{c}_{HE} = \frac{1}{2} Y_e g'^2 \left(\frac{16}{3} Y_q N_c c_{Hq}^{(1)} + \frac{8}{3} Y_u N_c c_{Ht} \right), \quad (3.20)$$

where Y_i is the hypercharge, $y_{t,b}$ are Yukawa couplings, and $N_c = 3$. These are all relevant RG equations that we include in this work.

Before discussing the scale choice, we comment on a few effects we have ignored. The RG evolution of c_6 is irrelevant as c_6 appears in only one observable at one energy scale – $\sigma(Zhh)$ at $\sqrt{s} = 500$ GeV. Thus, c_6 and the loop corrections to it cannot be distinguished. Likewise, c_{bH} and similar operators also appear in only one observable. Notably, c_{tH} mixes only with c_6 (Eq. (E.4)) and c_{bH} (Eq. (E.5)) among Higgs operators. It is not necessary to include the running of these Higgs operators. c_{3W} does not mix with any top operators. The RG effect of c_{Htb} is small as its RG contributions are proportional to y_b . We refer to Appendix E for complete expressions including \dot{c}_6 and \dot{c}_{bH} and contributions from bottom operators.

	G_F	EWPO	$\delta m_{W,Z,h,t}$	$\delta\Gamma(h)$	W^-W^+	$\sigma(\nu\bar{\nu}h)$	$\sigma(Zh)$	$\sigma(Zhh)$
Q_{proc} [GeV]	m_μ	m_Z, m_W	$m_{W,Z,h,t}$	m_h	250, 500	250, 500	250, 500	500

Table 2. The energy scales of observables, Q_{proc} . In our main results, EFT top-loop contributions are evaluated at $Q = \max(m_t, Q_{\text{proc}})$ in Eq. (3.22), but they are also compared with other choices of Q as explained in text. δm and $\delta\Gamma$ may appear in other observables but will still be evaluated at on-shell; examples are discussed in regard of Eq. (3.23). Q_{proc} for top production observables are not needed since top operators do not run in our analysis.

Some top-loop effects also arise from the renormalization of SM parameters (as discussed briefly in Section 3.4). Among SM parameters, only y_t, y_b, λ receive top-operator contributions. And only the running of y_t can be relevant to us because y_t can appear at multiple energy scales of m_t and $h \rightarrow \gamma\gamma, Z\gamma$, and later $t\bar{t}h$ (although we do not include it). The relevant RG equation is

$$\dot{y}_t = \frac{m_H^2}{v^2} \left(3y_t c_{tH} - y_t (c_{Hq}^{(1)} + 3c_{Hq}^{(3)} - c_{Ht}) - y_b c_{Htb} \right), \quad (3.21)$$

where m_H^2 is the quadratic mass parameter in the Higgs potential.

There are two distinct energy scales in the RG calculation. In this paper, Q_0 refers to the common scale that we use to express the Wilson coefficients, while Q refers to the renormalization scale for each physical process. In the following we discuss how the choices of the two scales affect the numerical results.

RG effects are evolved down from a common reference scale Q_0 . This scale can be set to the matching scale of new physics to the EFT, but formally it is arbitrary. In this work, it is just an arbitrary renormalization scale of Higgs and top Wilson coefficients c_i that we use to express theory predictions. The constraints on the Wilson coefficients $c_i(Q_0)$ from a global fit will depend on the choice of Q_0 . In Appendix D we show how the covariance matrix obtained at one scale can be evolved to another scale.

The bounds on physical observables (such as physical Higgs coupling precision) must be evaluated at their physical scales and the result must be independent of Q_0 . In Appendix D we prove that the results for the physical Higgs couplings are indeed independent of the choice of the reference scale Q_0 .

All RG contributions are evaluated at the renormalization scale Q of each observable. A natural choice is:

$$Q = \max(m_t, Q_{\text{proc}}), \quad (3.22)$$

where the top mass m_t is a natural scale below which top-loop effects are suppressed by the heavy top mass. Such decoupling of heavy-particle loop effects must be added

by hand in the mass-independent renormalization, e.g. with dimensional regularization and MS-bar subtraction scheme as in this paper. Q_{proc} is the characteristic energy scale of each observable, as collected in [Table 2](#). If $Q_{\text{proc}} < m_t$, operators renormalize only between m_t and Q_0 but not between Q_{proc} and m_t because the top quark is heavy and decouples. Of course, the decoupling scale is also somewhat arbitrary. In self-energy diagrams (e.g. second one in [Fig. 1](#)), $2m_t$ is a more relevant scale at which analyticity produces abrupt changes of loop functions. In the full-matching point of view, $\sqrt{2}m_t$ can be more relevant as the energy dependence of the gauge coupling beta function is highest there [\[44\]](#). All these choices are formally equivalent, but numerical differences just reflect the fact that we are terminating at some finite order in perturbative expansion. Therefore, we use the choice in [Eq. \(3.22\)](#) as a main one throughout the paper. A comparison with alternative choices, such as $Q = \max(2m_t, Q_{\text{proc}})$ and $Q = Q_{\text{proc}}$, is presented in [Appendix C](#).

Lastly, observables often involve multiple energy scales. For example,

$$\delta\sigma(Zh \rightarrow Zb\bar{b})(Q_{\text{proc}} = 250) = \delta\sigma(Zh)(250) + \delta\Gamma(b\bar{b})(m_h) - \delta\Gamma_{\text{tot}}(m_h), \quad (3.23)$$

where numbers in parentheses are Q_{proc} values. Further, $\delta\Gamma$ may depend on, e.g. the Z boson mass δm_Z which will always be evaluated at $Q_{\text{proc}} = m_Z$. In the end, the observable $\delta\sigma(Zh \rightarrow Zb\bar{b})$ will be written in terms of $c_i(Q_0)$ at Q_0 and the covariance matrix of $c_i(Q_0)$ is obtained. The explicit Q_0 dependence of the matrix can be used to derive final constraints on the coefficients at some common reference scale Q_0 .

3.6 Finite one-loop effects of top couplings

Several Higgs observables receive effects from top operators that are not logarithmic one-loop. The operator coefficient c_{tH} that shifts the top Yukawa coupling ([Section 3.3](#)) affects $h \rightarrow \gamma\gamma$, gg , $Z\gamma$ decays at one-loop (without UV divergences, hence without log-enhancements) and $pp \rightarrow t\bar{t}h$ and $e^+e^- \rightarrow t\bar{t}h$ production rate at tree-level. In addition to the modifications due to Higgs operators and SM parameter variations, c_{tH} modifies these observables as follows:

$$\delta\Gamma(h \rightarrow \gamma\gamma) = \text{Re} \left(\frac{A_{\text{top}}}{A_{\text{top}} + A_W} \right) 2c_{tH} + \dots, \quad (3.24)$$

$$\delta\Gamma(h \rightarrow gg) = 2c_{tH} + 2c_{gH} + \delta Z_h, \quad (3.25)$$

$$\delta\sigma(t\bar{t}h) = 2c_{tH} + \dots, \quad (3.26)$$

where $A_{\text{top},W}$ are SM amplitudes with top and W loops, and \dots are from the variations other than c_{tH} calculated in [\[1\]](#) and [\[15\]](#). In $\delta\Gamma(h \rightarrow gg)$, we write the full expression separating c_{tH} from c_{gH} , which were altogether described by a single parameter c_{gH}

in [1]. In this work, c_{tH} affects various observables differently from c_{gH} . Hence, the two operators can be distinguished from each other. Numerical evaluations of these expressions are collected in Table 10 – 12. The loop diagrams for $h \rightarrow \gamma\gamma$ and $h \rightarrow Z\gamma$ in Fig. 2 can also be mediated by a W -boson. This introduces a dependence of the decay rates on electro-weak couplings. This dependence is accounted for in our fit.

The $h \rightarrow Z\gamma$ decay rate is affected by modifications of both the top Yukawa coupling and the $Zt\bar{t}$ coupling. The operator coefficients $c_{Hq(3), Hq(1), Ht}$ shift the vectorial part of $Zt\bar{t}$ vertex (and $Zb\bar{b}$ similarly) as follow:

$$\mathcal{L} = \frac{g}{c_w} Z^\mu \bar{t} \gamma_\mu t (\ell + r) \left(1 + \frac{-c_{Hq}^{(1)} + c_{Hq}^{(3)} - c_{Ht}}{2(\ell + r)} \right) \equiv \frac{g}{c_w} Z^\mu \bar{t} \gamma_\mu t (\ell + r) (1 + c_{Ztt}), \quad (3.27)$$

where $\ell = \frac{1}{2} - \frac{2}{3}s_w^2$ and $r = -\frac{2}{3}s_w^2$. The tree-level shift $(1 + \delta y_t + c_{Ztt})$ modifies the top-loop of $\delta\Gamma(h \rightarrow Z\gamma)$ in the same way as $\delta\Gamma(h \rightarrow \gamma\gamma)$ in Eq. (3.24) so that

$$\delta\Gamma(h \rightarrow Z\gamma) = \text{Re} \left(\frac{A_{\text{top}}^{Z\gamma}}{A_{\text{top}}^{Z\gamma} + A_W^{Z\gamma}} \right) 2(c_{tH} + c_{Ztt}) + \dots \quad (3.28)$$

Numerically, this effect is rather small because the top-loop SM contribution to $h \rightarrow Z\gamma$ (denoted by $A_{\text{top}}^{Z\gamma}$) is much smaller than the W -loop's $A_W^{Z\gamma}$. We comment that c_{tW} seems to also shift the $Zt\bar{t}$ coupling, but this is UV divergent and is actually renormalizing c_{WW} rather than tree-level shifting the coupling.

Lastly, we emphasize again that we include finite one-loop effects in Eq. (3.24), (3.25), and (3.28) because SM contributions are also at one loop so that top effects are at the same level, without an effective loop suppression.

3.7 Summary

The basis for our combined EFT fit to Higgs/EW and top physics data has 29 degrees of freedom. These include eight + one Higgs operator coefficients:

$$c_{H, T, WW, WB, BB, HE, HL, HL', 3W}, \quad (3.29)$$

seven top operator coefficients:

$$c_{Ht, HQ(1), HQ(3), tH, tB, tW, Htb}, \quad (3.30)$$

five coefficients for four Yukawa operators and one operator for $h \rightarrow gg$:

$$c_{bH, cH, \tau H, \mu H, gH}, \quad (3.31)$$

four coefficients for non-standard Higgs decays:

$$a_{\text{inv}}, a_{\text{oth}}, \mathcal{C}_{W,Z}, \quad (3.32)$$

and four SM parameters (electroweak gauge couplings, Higgs vacuum expectation value, and Higgs self interaction):

$$\delta g, \delta g', \delta v, \delta \bar{\lambda}. \quad (3.33)$$

The computed numerical expressions of each observable in terms of operator coefficients are collected in [Appendix F](#).

4 Benchmark datasets

To study the interplay between Higgs/EW and top measurements and operators we perform fits on several benchmark data sets. The benchmarks include LEP/SLC electro-weak precision measurements, LHC results in Higgs and top physics, and prospects for Higgs/EW and top physics for the high-luminosity phase of the LHC (HL-LHC) and for the ILC runs at $\sqrt{s} = 250$ GeV and 500 GeV. In this section we provide a brief overview of these scenarios.

The SM parameter values that we use in our fits are from central values of the measurements:

$$\begin{aligned} m_Z &= 91.1876 \text{ GeV}, & m_W &= 80.385 \text{ GeV}, & m_h &= 125.090 \text{ GeV} \\ m_t &= 173 \text{ GeV}, & m_b &= 4.3 \text{ GeV}, & m_\mu &= 0.105 \text{ GeV} \\ s_w^2 &= 0.23152, & \alpha^{-1} &= 128.9220 & v &= 246 \text{ GeV}. \end{aligned} \quad (4.1)$$

Here, $m_{t,b}$ come in as $y_{t,b}$ in RG equations, while m_μ provides the scale Q for G_F .

4.1 LEP/SLC electro-weak precision observables

Nine electroweak precision observables are collected in [Table 3](#). The uncertainties are set to the currently available LEP/SLD measurements [\[45\]](#). Expected improvements from the LHC and ILC are included for m_W, m_h, Γ_W , and A_ℓ , as in Ref. [\[19\]](#). This baseline set of electro-weak precision observables (EWPOs) is included in all benchmark scenarios. Numerical values are given in [Table 3](#). For some fits we consider the Tera-Z precision [\[6\]](#) listed in the same table. All values are in agreement with those in Ref. [\[19\]](#), except for one. We consider the improvement in A_ℓ that can be achieved with a radiative-return analysis at the ILC, which was not considered in Ref. [\[19\]](#).

observable unit	$\alpha^{-1}(m_Z^2)$ -	G_F (GeV ⁻²)	m_W (MeV)	m_Z (MeV)	m_h (MeV)	A_l (%)	Γ_l (MeV)	Γ_Z (MeV)	Γ_W (MeV)
LEP/SLC	0.0178	0.6×10^{-10}	15	2.1	240	0.13	0.086	2.3	42
+LHC/ILC	idem	idem	5	idem	15	0.013	idem	idem	2
+Tera-Z	0.00387	idem	0.5	0.1	idem	0.004	0.0054	0.1	1.2

Table 3. Summary of the uncertainties on electro-weak precision measurements, as included in the fits. The first line (LEP/SLC) lists the current constraints. The second line (LHC/ILC) includes expected improvements at the LHC and the first stage of the ILC. The third line reflects the precision envisaged for a Tera-Z programme at a circular e^+e^- collider. The uncertainties labelled +LHC/ILC form the baseline scenario included in all fits. The value denoted by “idem” is identical to that in the earlier row.

4.2 Selected LHC Higgs measurements

Three ratios of Higgs branching ratios are included from the LHC. For rare decays, the LHC prospects after the full high-luminosity phase are very competitive [46]. As systematic errors largely cancel, these ratios are expected to improve with statistics as $1/\sqrt{N}$. Expectations are taken from the HL-LHC prospects [47] for 3 ab^{-1} : $\text{BR}(ZZ^*)/\text{BR}(\gamma\gamma) \sim 2\%$, $\text{BR}(Z\gamma)/\text{BR}(\gamma\gamma) \sim 20\%$, and $\text{BR}(\mu^+\mu^-)/\text{BR}(\gamma\gamma) \sim 8\%$. This precision exceeds what was assumed in Ref. [19], that was based on the more conservative ATLAS study [46]. This set of results is included in all three benchmark scenarios.

4.3 LHC top production - run 2

Measurements are included of a variety of processes that are sensitive to top electro-weak couplings, including associated $t\bar{t} + V/h$ production, electro-weak single-top production, and top-decay. The analyses of the LHC run 2 data set are based on 36 fb^{-1} at $\sqrt{s} = 13 \text{ TeV}$. The top decays analysis is performed with 20 fb^{-1} at $\sqrt{s} = 8 \text{ TeV}$. The constraints are based on the analysis in Ref.[15]. The $t\bar{t}$ and hh production rates are not used, but they are implicitly assumed to constrain the one-loop effects of c_{tG} and c_6 , respectively.

4.4 HL-LHC top production - S2 scenario

The same measurements and final states are included as in the run 2 scenario above, where uncertainties are extrapolated to the total integrated luminosity of 3 ab^{-1} at 14 TeV envisaged in the high-luminosity stage of the LHC. The statistical uncertainties and experimental systematics are expected to scale as $1/\sqrt{N}$, while the current theory uncertainties on SM predictions are divided by two.

4.5 ILC Higgs/EW measurements at $\sqrt{s} = 250$ GeV

This data set includes Higgs and EW observables. The W^+W^- production process is used to constrain Triple Gauge boson Couplings (TGCs). Higgs measurement include the results of the Higgsstrahlung ($e^+e^- \rightarrow Zh$) recoil mass analysis (total and differential cross sections, and cross section times branching ratios) and an analysis of the Vector Boson Fusion (VBF) channel ($e^+e^- \rightarrow \nu\bar{\nu}h, h \rightarrow b\bar{b}$). A total integrated luminosity of 2 ab^{-1} is shared equally between two beam polarizations ($\pm 30, \mp 80$). The uncertainties are given in Ref. [19].

4.6 ILC Higgs/EW measurements at $\sqrt{s} = 500$ GeV

The same observables are used as in the ILC250 scenario, plus seven $\sigma \times BR$ measurements in the VBF channel. The ILC500 stage envisages a total integrated luminosity of 4 ab^{-1} . Uncertainties are given in Ref. [19].

4.7 ILC top quark pair production at $\sqrt{s} = 500$ GeV

This projection includes measurements of a set of optimal observables [20] in $t\bar{t}$ production at $\sqrt{s} = 500$ GeV (4 ab^{-1} with two beam polarizations). The results are presented in Appendix C.2.5 of [15]. Associated $t\bar{t}h$ production is considered separately, with a 13% uncertainty on the cross section at $\sqrt{s} = 500$ GeV, which can be improved to 6% at $\sqrt{s} = 550$ GeV [15].

5 Global-fit analysis

5.1 Method

We perform a global fit to find the optimal values and projected uncertainties for the 29 degrees of freedom listed in Section 3.7. From the results, we also reconstruct the projected uncertainties on physical Higgs couplings and top Yukawa as the combined errors on $\delta g(hXX)$ (Eq. (3.3)) and δy_t (Eq. (3.10)), respectively.

The global fit minimizes the total χ^2

$$\begin{aligned} \chi^2 &= \sum_{m,n} (\hat{O}_{exp} - \hat{O}_{thy})_m (\sigma^{-2})_{mn} (\hat{O}_{exp} - \hat{O}_{thy})_n \\ &= \sum_{I,J} c_I(Q_0) \mathcal{Cov}_{IJ}^{-1}(Q_0) c_J(Q_0), \end{aligned} \tag{5.1}$$

where m, n specify observables and σ_{mn} is a matrix of error correlations among observables. Theory predictions in terms of operator coefficients at Q_0 turn the correlation matrix into the covariance matrix of operators at Q_0 , $\mathcal{Cov}(Q_0)$, with operator indices

I, J . The fact that the observables can be expressed in terms of the coefficients at any scales implies that the $Cov(Q_0)$ at one scale Q_0 is physically equivalent to the $Cov(Q'_0)$ at another scale Q'_0 , connected by the RG evolutions of operators; see [Appendix D](#) for detailed discussions and examples. Our covariance matrices for benchmark scenarios are collected in [Appendix H](#).

5.2 Results for the ILC at $\sqrt{s} = 250$ GeV

In this section, we compare several fits on the initial ‘‘Higgs factory’’ stage of the ILC, which collects 2 ab^{-1} at $\sqrt{s} = 250$ GeV. The benchmark data set for this fit includes the baseline EWPO described in [Section 4.1](#), the measurements of rare Higgs branching ratios at the LHC of [Section 4.2](#) and the ILC Higgs/EW data of [Section 4.5](#). The fits on the extended basis include also LHC measurements of the top quark EW couplings, either at the current run 2 precision ([Section 4.3](#)) or the projected precision for the full HL-LHC program in scenario S2 ([Section 4.4](#)).

The results of these fits are presented in [Fig. 3](#). The upper panel presents the expected precision of the physical Higgs couplings (defined as the 1σ constraint on the square root of the decay width ([Section 3.1](#)); $\delta\bar{\lambda}$ and δy_t are defined in [Eq. \(3.5\)](#) and [Eq. \(3.10\)](#), respectively). The Higgs coupling precision is evaluated at $Q_{\text{proc}} = m_h$, and the result is independent of Q_0 (see [Appendix D](#)). The lower panel presents the 1σ bounds on the operator coefficients. The operator coefficients are renormalized at $Q_0 = 1$ TeV with a suppression scale v .

For each coupling or operator, three results are presented. The result labeled as ‘‘w/o top’’ is intended for reference: it corresponds to the 22-parameter fit of [Ref. \[19\]](#) without top operators ⁷. The second bar, labeled ‘‘w/top + LHC run 2’’ corresponds to a fit with the complete 29-parameter basis including top operators of [Section 3.7](#). To ensure convergence of the fit, it includes the current LHC run 2 top physics data of [Section 4.3](#); global fits do not converge without top data as too many parameters need to be determined. The last bar, ‘‘w/top + HL-LHC S2’’, includes the expected improvements in top physics of the HL-LHC scenario ‘‘S2’’ of [Section 4.4](#).

Remarkably, the ILC precision on the physical Higgs couplings remains robust against model-independent top effects. The global fits with 22 parameters (without tops) and 29 parameters (with tops) yield similar precision. The most pronounced deterioration is observed in the hZZ and hWW couplings in the ‘‘LHC run 2’’ scenario, where the precision degrades by 0.48% and 0.62%, respectively. The parameter $\bar{\lambda}$ degrades by 40%. The precision of the Higgs coupling measurements improves again

⁷The relevant typos in [Ref. \[19\]](#) are collected in [Appendix A](#) and are corrected in the fit presented in this paper.

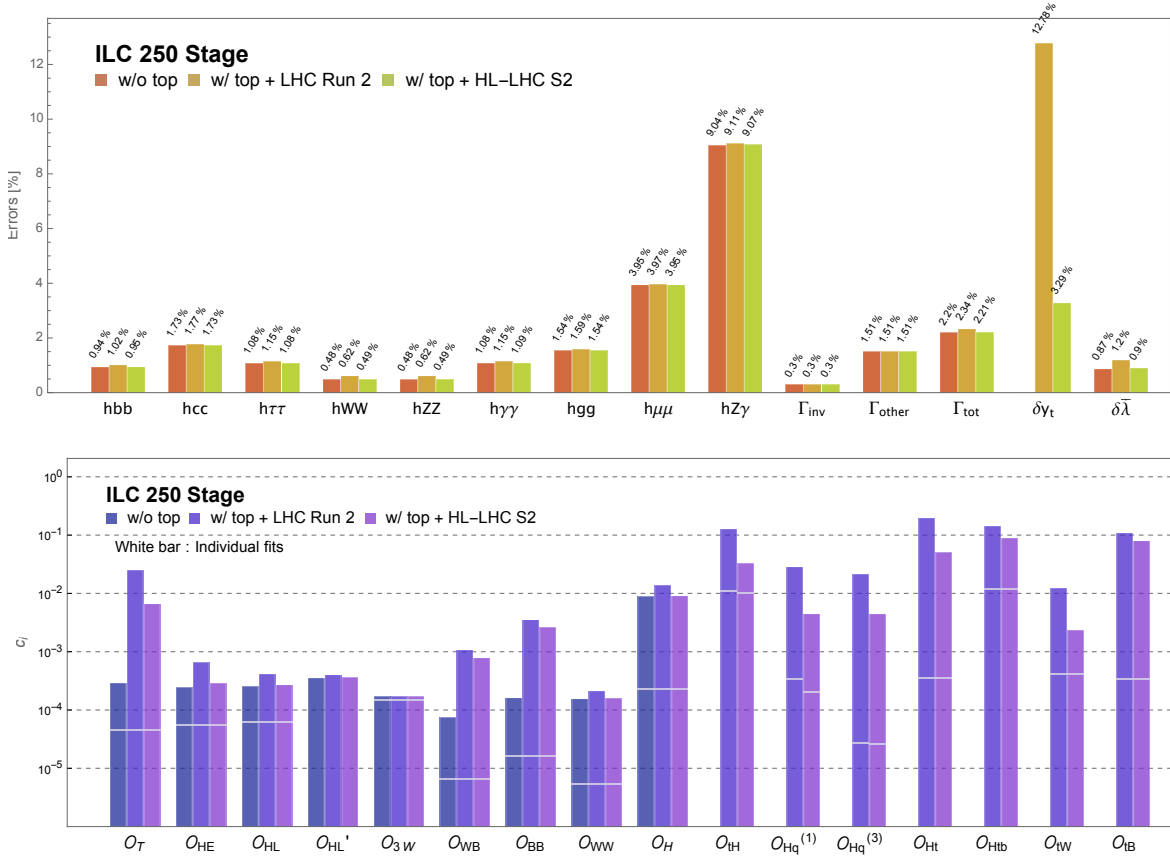


Figure 3. Global fit results for the ILC 250 scenario. The upper panel presents the result in terms of the precision on the physical Higgs couplings (Eq. (3.3)). The lower panel presents the 1σ bounds on the operator coefficients, renormalized at $Q_0 = 1$ TeV with a suppression scale v . RG contributions are evaluated at $Q = \max(m_t, Q_{\text{proc}})$ as in Eq. (3.22) and Table 2. In both panels, the first column corresponds to a 22-parameter fit without top operators [19], used as a reference throughout the paper. The second column presents the result that is obtained when the basis is extended with the seven top operator coefficients described in Section 3.2 and LHC run 2 data are added. The last column repeats the same fit with the expectations of the S2 scenario for the measurement of the top quark electro-weak couplings at HL-LHC. In the bottom panel, white marks are results with only one operator. Results are tabulated in Table 13 and 14.

with the inclusion of stronger top production data from HL-LHC, almost to the level without top effects.

The robustness of the bounds on the physical Higgs couplings is understood as follows. The renormalization scale $Q = \max(m_t, Q_{\text{proc}})$ for top-loop effects is m_t for many

observables, including Higgs decay widths with $Q_{\text{proc}} = m_h < m_t$ and EWPOs with $Q_{\text{proc}} = m_Z < m_t$. Thus, those observables depend on common combinations of Higgs operators and their RG corrections by top operators: $\tilde{c}_i(m_t) = c_i + \frac{1}{16\pi^2} \gamma_{ij} c_j(Q_0) \log \frac{m_t}{Q_0}$ (Eq. (3.12)). In the limit where only a single scale Q is relevant, all top effects appear through $\tilde{c}_i(Q)$ so that one can redefine all Higgs operator coefficients c_i by fixed combinations $\tilde{c}_i(Q)$. Physical Higgs couplings will then depend only on \tilde{c}_i in the same way they depended on c_i in the global fit without top operators. Then the global fit results for physical Higgs couplings with top operators must be equivalent to the one without top operators. If all observables are at similar scales, one expects that the Higgs coupling precision is robust against the extension of the basis with the top operators. In Appendix C, we present fit results for several different choices of the scale Q , corroborating this explanation. In other words, the heaviness of the top quark makes the Higgs coupling precision rather insusceptible to model-independent top effects.

This is remarkable. RG effects are discernible from tree-level effects through the measurements at multiple energy scales because RG effects vary with the energy scale while tree-level effects remain constant. Thus, one may expect that measurements at multiple energy scales are the ones responsible to help achieve high precision in global-fit analyses. However, we just saw a very different conclusion; having many observables with common energy scales actually allows to measure certain combinations of tree-level and RG effects (appearing at the common scale) more precisely. This resulted in the robust Higgs coupling precision at the ILC.

On the other hand, by actually the same reason, the constraints on operator coefficients degrade much more significantly with top effects, as shown in the bottom panel of Fig. 3. In the presence of top operators, it is difficult to constrain individual operators that combine into physical Higgs couplings. But many common scales (that made Higgs coupling precision robust) do bother disentangling tree-level effects of Higgs operators and RG effects of top operators. The degeneracies between them are not well resolved by Higgs+EW data at 250 GeV alone. Only with the higher-precision top production data of the HL-LHC S2 scenario, the degeneracies are reduced and operators are better constrained in the global fit. However, the precision does not fully recover to the level of the reference fit at the ILC 250 stage.

Apparently, the two panels of Fig. 3 would seem to lead to different conclusions. While the physical Higgs couplings are affected by 30% to 40% at most, the bounds on operator coefficients can degrade by orders of magnitudes. The projection onto the physical Higgs couplings can be useful because they are robustly and semi-directly measured and theoretical predictions of Higgs coupling deviations in various new physics models are available. But these are not full information of new physics effects. The projection onto the operator constraints is still needed to pinpoint the origin of the

deviations and to distinguish new physics models.

Lastly, we discuss one feature shown in Fig. 3. The Higgs couplings that seem to be most sensitive to top effects are $g(hWW)$, $g(hZZ)$ and $\bar{\lambda}$, as shown in the second bars. This is related to the worsening of $c_{T,WB,BB}$ constraints, as shown in the bottom panel. Why are these operators particularly sensitive to top effects? c_T RG mixes most strongly with top operators, in particular with c_{Ht} ⁸, and $c_{WB,BB}$ strongly with c_{tB} ⁹. These top operators are also not well constrained.

All in all, the ILC precision of the physical Higgs couplings are remarkably robust against the presence of poorly constrained top operators that affect the Higgs measurements through top-loop effects. However, even if the physical couplings of the Higgs boson are well constrained, strong degeneracies or “blind directions” may be present in the basis of operator coefficients that prevent an unambiguous new physics interpretation of the result. Therefore, precise measurements of the top-quark EW couplings are important to take full advantage of the ILC Higgs factory stage.

5.3 The role of beam polarization

The possibility of highly polarized beams is one of the distinguishing features of linear colliders. It is instructive to compare the impact of top operators on the model-independent precision measurements with and without beam polarization. The one with polarization represents linear e^+e^- colliders while the other represents circular e^+e^- colliders. Following Ref. [19], we compare those results in Fig. 4. The results labeled “polarized” are for the ILC 250 benchmark scenario of Fig. 3, consisting of 1 ab^{-1} for each of the two beam polarizations; the results labeled “unpolarized” include Higgs measurements in 5 ab^{-1} without beam polarization and the improved Tera- Z estimates for the Z -pole EWPO (as described in Section 4.1). The light and dark shadings represent the results with and without top operators. In the 29-parameter fit with top operators, HL-LHC S2 top production is included for both polarized and unpolarized scenarios.

As shown in the figure, the power of beam polarization is not significant in terms of the robustness against top effects. The Higgs coupling precisions are all robust irrespective of the existence of beam polarization, as expected from the discussion in Section 5.2. The operator constraints are slightly more robust in the polarized scenario, but the difference is not large. As an interesting remark, the polarization effects become more pronounced if we had used $Q = Q_{\text{proc}}$, where more various scales are involved;

⁸ $c_{Hq}^{(1)}$ also RG mixes, but it is better constrained than c_{Ht} (Fig. 3) by $b\bar{b}$ observables at LEP and LHC [15].

⁹ c_{tW} is better constrained than c_{tB} by top-decay and single-top measurements at LHC [15]. It is also why c_{WW} (mixing with c_{tW} but not with c_{tB}) is not degraded as much as $c_{WB,BB}$.

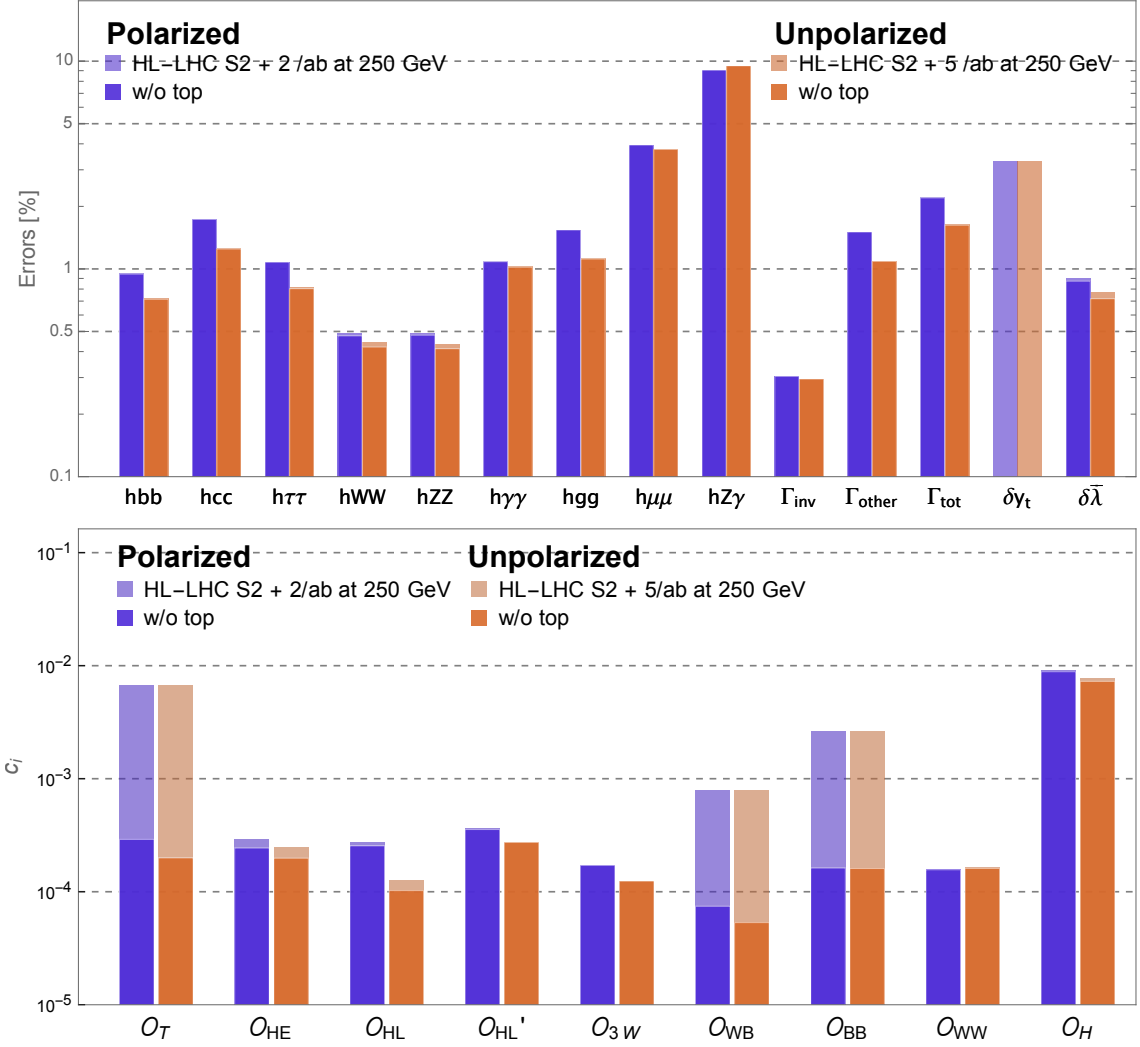


Figure 4. The role of beam polarization at $\sqrt{s} = 250$ GeV on the Higgs coupling precision (upper) and Higgs operator constraints (lower) with (light shading) and without (dark shading) top effects. The polarized (blue) dataset includes equal sharing of two opposite beam polarizations (1 ab^{-1} each) of ILC, and the unpolarized (red) includes a higher luminosity of 5 ab^{-1} and enhanced Tera- Z precision for EWPO. HL-LHC S2 top data is added.

see [Appendix C](#). The beam polarization effectively doubles the number of independent observables, which allows to better disentangle top and Higgs contributions.

5.4 The role of electro-weak measurements

In Fig. 5 we assess the importance of the EWPO and TGC datasets in the global fit by varying the precisions of EWPO and TGC measurements. The height of the bars indicates the ratio of the bounds obtained with the current LEP/SLD precision and with future precisions of ILC250 (except Tera-Z for unpolarized EWPO). Thus, the bars show improvements of global-fit results obtained from the improvement of EW dataset. The exact dataset values used are collected in Table 3. The three bars show different global fits: the first on the reference fit without top operators, and the last two on the fits with top operators including either current LHC run 2 or future HL-LHC S2 bounds on top EW couplings.

The EW measurements generally become less powerful in the presence of top operators in particular when the top operators are relatively not well constrained at LHC run 2; this can be seen as much smaller heights of the second bars. The degeneracies between Higgs and top effects are one of the bottlenecks for taking advantage of the EW precision measurements. As the degeneracies can be reduced by tighter constraints on the top operators from HL-LHC, the importance of EW/TGC dataset also increases. This means that top data and EW/TGC data are complementary or somewhat orthogonal in resolving those degeneracies; but EWPO and TGC alone are not powerful enough to remove those degeneracies. The EW measurements are more important for unpolarized lepton colliders as beam polarization doubles the independent set of observables. The importance is also more pronounced on operator constraints since EW/TGC dataset can directly constrain some operators and reduce degeneracies between operators.

Among all EW observables, the Higgs mass is the most influential one in global fits. White markers indicate the results that are obtained with δm_h fixed to the future LHC/ILC precision of 15 MeV, while all other EWPO continue to vary. These results show that most of the precision improvement from EWPO comes from the improvement of δm_h . This is in agreement with Ref. [48] that did not even consider top effects, implying that the Higgs mass is most important regardless of model-independent top effects. Finally, the further improvement of δm_h from the 15 MeV does not bring additional improvements of global fits at ILC 250.

In summary, the improvements of EW/TGC dataset from the current LEP/SLD precision to the future LHC/ILC precision are very important for the global fits, as well as strong bounds on the top-quark electro-weak operators.

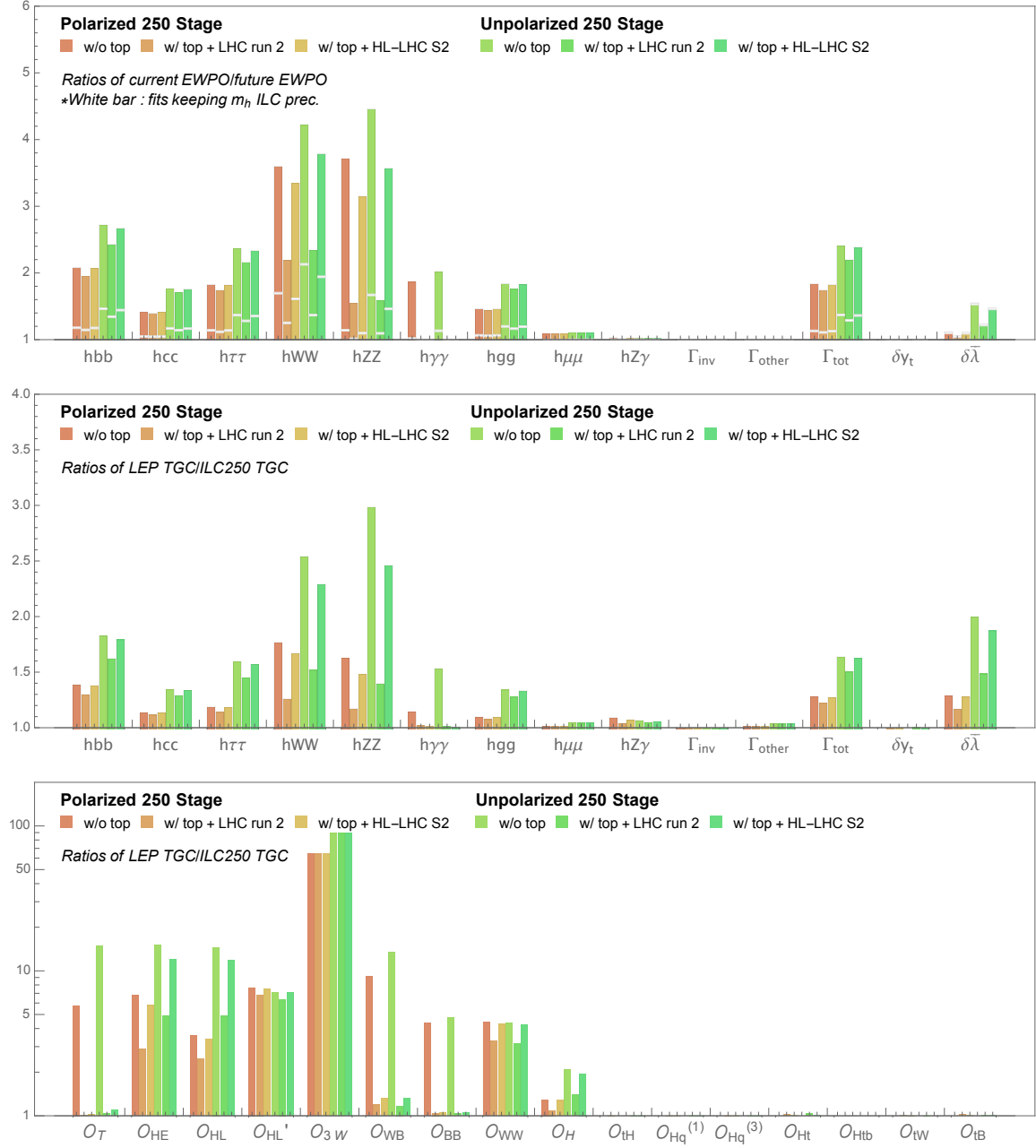


Figure 5. The ratio of Higgs coupling precision obtained by varying EWPO and TGC uncertainties, from current LEP/SLD uncertainties of EWPO (upper panel) and TGC measurements (central panel) to the future uncertainties of ILC250 (Tera- Z for unpolarized EWPO). The white markers indicate the results with the uncertainty δm_h fixed to the future LHC/ILC precision of 15 MeV while all other EWPO uncertainties varied. The third panel presents the results of the variation of the TGC precision in the operator basis. The first three columns are with polarized dataset, and the last three are with unpolarized.

5.5 Results for higher-energy operation – ILC 500 stage

The nominal ILC programme includes 2 ab⁻¹ at $\sqrt{s} = 250$ GeV and 4 ab⁻¹ at $\sqrt{s} = 500$ GeV. The Higgs measurements at higher energy, with much more abundant VBF production, lead to a significantly improved Higgs fit [1]. The sensitivity of measurements in $e^+e^- \rightarrow W^+W^-$ increases with center-of-mass energy. And, finally, the high-energy run opens up top quark pair production, allowing for a precise characterization of the electro-weak interactions of the top quark [15, 20, 49].

The results of a fit to the combined ILC250+ILC500 scenario are presented in Fig. 6. The upper and lower panels again correspond to the physical Higgs coupling basis and the effective operator coefficients. For each coupling precision and operator constraint, four results are shown. The first bar corresponds to the 22-parameter reference fit to the two ILC stages of Ref [19]. The second, third and fourth bar are obtained with the full 29-parameter basis. The second bar uses only Higgs and EW observables, the third adds the HL-LHC top constraints in the S2 scenario, and the fourth adds the constraints on top EW operators from the ILC run at $\sqrt{s} = 500$ GeV.

Notably, global fits in the 29-parameter basis now converge without top production data (second bar). The dataset with two ILC energy stages provides a sufficiently rich set of measurements to constrain also the top operator coefficients. However, the Higgs coupling precision in this case is significantly degraded with respect to the reference fit, and indirect constraints on top operators remain much worse than those from measurement in top production. Higgs coupling precision without top production data is not as robust as in ILC250 since ILC500 now provides a new energy scale so that the degeneracies with top effects become more important. Adding ILC 500 top production data (fourth bar) can almost fully recover the Higgs coupling precision. HL-LHC top data is also useful, but not quite sufficient to restore the precision to that of the reference fit without top operators.

A more remarkable impact is found in the basis of operator coefficients. In particular, the coefficients $c_{Ht,tB}$ and $c_{T,WB,BB}$, which mix strongly with each other, are strongly affected. The mixing consequently affects the precision of λ and $g(hZ\gamma)$ too. Only in the last scenario, including ILC 500 top data, the degeneracies between Higgs and top operators are fully resolved and all operators and couplings are constrained as well as in the reference fit without top operators.

All in all, ILC 500 is capable of precise and the model-independent test of the SMEFT with top effects. The precision of the top electro-weak coupling measurements at the HL-LHC and in $e^+e^- \rightarrow t\bar{t}$ is essential for model-independent Higgs coupling precision.

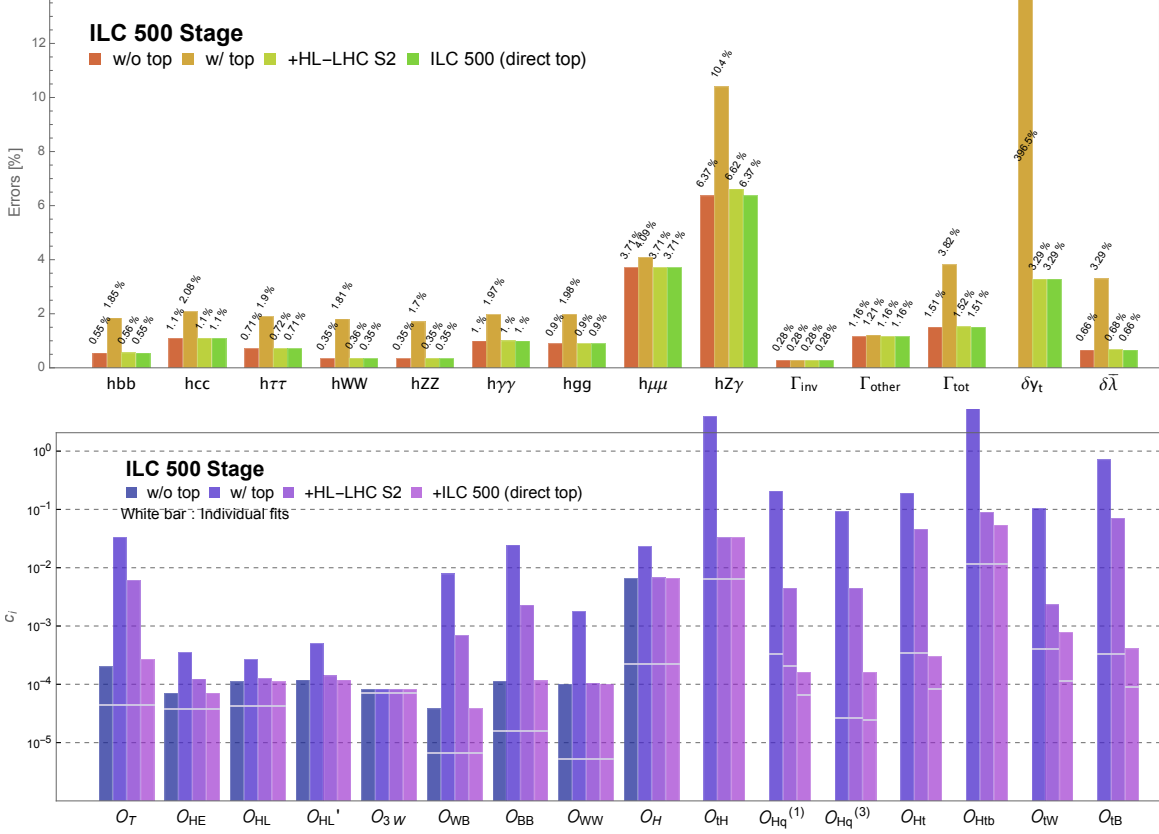


Figure 6. Global-fit results for the ILC250+ILC500 scenario. The upper panel presents the result in terms of the precision on the physical Higgs couplings. The lower panel presents the 1σ bounds on the operator coefficients, renormalized at $Q_0 = 1$ TeV with a suppression scale v . In both panels, the first column corresponds to a 22-parameter fit without top operators, that is used as a reference throughout the paper. The second column presents the result that is obtained when the basis is extended with the seven top operator coefficients described in Section 3.2. In the third column, LHC run 2 top data are added. In the fourth column, ILC top measurements at $\sqrt{s} = 500$ GeV are added. In the bottom panel, white marks are results with only one operator. Results are tabulated in Table 13 and 14.

		$\langle(\delta\sigma(Zhh))^2\rangle^{1/2}$
w/o top op.	ILC 250	2.66%
	ILC 250 + 500	2.13%
w/top op.	ILC 250 + 500 (Higgs/EW)	8.06%
	+ HL-LHC top	2.62%
	+ ILC 500 top	2.13%

Table 4. Total uncertainties of the $\sigma(Zhh)$ contributed from EFT operators, evaluated at $Q = 500$ GeV. Measurement uncertainties are estimated to be 16% [8, 53] but not shown. These results are independent on Q_0 (Appendix D). The first two rows correspond to the fit on the 22-parameter basis without top operators, for ILC Higgs/EW data at $\sqrt{s} = 250$ GeV and for the complete programme at 250 + 500 GeV. The three last rows correspond to the 29-parameter fit on the complete basis with top operators. The first of them includes Higgs/EW data only, while the second and third add top physics measurements at the HL-LHC and ILC500, respectively.

5.6 The Higgs self-coupling

The triple coupling or self-coupling of the Higgs boson is one of the key objectives of high-energy physics in the next decades [50]. A robust extraction of this parameter is an important consideration in the design of the Higgs factory and its operating scenarios [1, 32, 33, 51].

The Higgs self-coupling λ and the operator coefficient c_6 are expected to be measured in di-Higgs boson production at the LHC before the ILC turns on [50]. However, a model-independent extraction from LHC data is difficult. One of the most challenging aspects is that the $gg \rightarrow hh$ process receives contributions from several diagrams. In addition to the diagram with a triple-Higgs-boson vertex, box and loop diagrams involving $t\bar{t}h$ vertices yield sizeable contributions to the total rate. This results in a strong dependence on several operator coefficients, among which c_{tH} [52].

In our EFT fit, as discussed at the end of Section 3.4, the Higgs self-coupling λ and c_6 appear together in the $\bar{\lambda}$ parameter (Eq. (3.5)), which is constrained by measurement of the Higgs mass. Figure 6 shows that the reference result $\delta\bar{\lambda} = 0.66\%$ of the 22-parameter fit at ILC500 is degraded to 3.29% when the basis is extended with top operators. The precision recovers to 0.68% after inclusion of HL-LHC top data in the S2 scenario, and fully recovers with the top measurements in $e^+e^- \rightarrow t\bar{t}$ production at ILC500.

Even if the $\bar{\lambda}$ coefficient is tightly bounded, we cannot constrain λ and c_6 individually with the 250 GeV data alone (remember that finite loop effects from the Higgs

operator on the Zh cross section are not included in the fit). The coefficients c_6 is precisely measured by $\sigma(Zhh)$ at ILC500. This measurement separates the two parameters, since λ and c_6 enter in different combinations in that process. Here, we evaluate the effect of Higgs and top operator coefficients on the extraction of c_6 .

Table 4 shows the total uncertainty on the cross-section $\delta\sigma(Zhh)$ from EFT coefficients. This EFT error contribution in the model-independent extraction of c_6 must be kept small - by precise measurements of single-Higgs and top production rates - to convincingly attribute a measured deviation in the double Higgs production cross section to a shift in the triple Higgs coupling. The errors are evaluated at $Q = 500$ GeV, and the results are independent of the choice Q_0 .

With only Higgs+EW data, the EFT uncertainty contribution is 8.06%, better than the expected measurement error of 16% [8, 53]. This means that the measurement of c_6 from $\sigma(e^+e^- \rightarrow Zhh)$ is robust, even in the presence of top operators. Addition of the HL-LHC top production data improves the uncertainty to 2.6%. Finally, $e^+e^- \rightarrow t\bar{t}$ at $\sqrt{s} = 500$ GeV fully recovers the constraint 2.13% of the reference fit without top operators.

An interesting aside is that, even though the final errors are 2.13% both with or without top operators, individual EFT contributions to the total error are quite different. In the fit on the extended basis, c_T becomes the dominant source of EFT uncertainties while c_H was the dominant contribution before top operators were added.

In summary, the extraction of the Higgs boson self-coupling from the di-Higgs production rate at the ILC at $\sqrt{s} = 500$ GeV is robust against the impact of other Higgs operators and top operators. With the inclusion of HL-LHC and ILC500 results on top electro-weak couplings, the effect of those operators on the extraction is reduced to well below the expected measurement uncertainty.

5.7 Indirect bounds on top-EW couplings

The effect of the top operator coefficients on the Higgs and EW observables offers a way to probe these operators during the first ‘‘Higgs factory’’ stage of the ILC project at $\sqrt{s} = 250$ GeV, when the top quark pair production process is not yet accessible. The indirect bound from the Higgs/EW fit is therefore the first top quark physics of the new project.

The individual bounds on all operator coefficients from a fit to the ILC500 projection are presented in Fig. 7. The measurements are grouped in two broad categories: electro-weak precision measurements and Higgs coupling measurements. These indirect determinations are compared to the projections for HL-LHC top physics results in the S2 scenario and to the bounds expected from ILC top measurements at $\sqrt{s} = 500$ GeV.

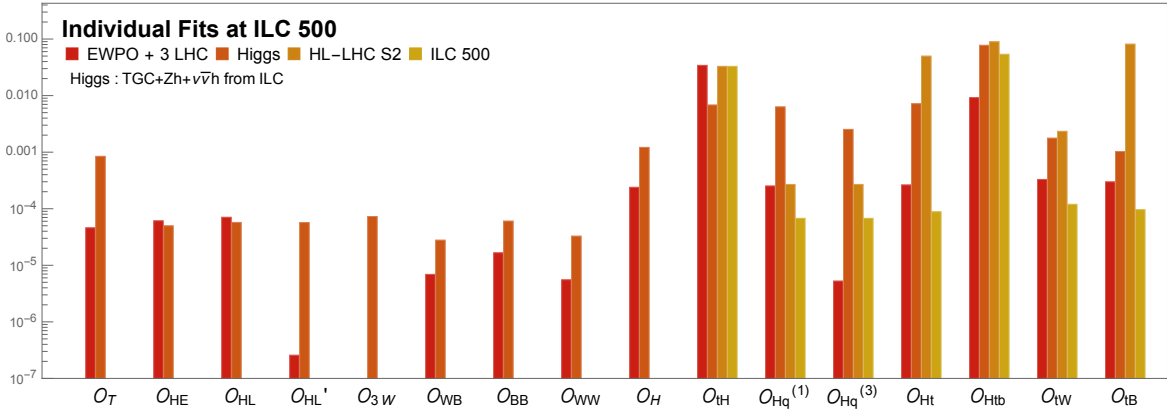


Figure 7. The individual constraints on the EFT coefficients by each set of measurements at ILC 500 and HL-LHC stages. The first column (EWPO+3 LHC) shows the individual bounds by 9 EWPOs and 3 branching ratios measurements from LHC. The second column (Higgs) is from the TGC measurements and Higgs production processes ($Zh + \nu\bar{\nu}h$) from ILC. The third and fourth ones represent those from direct top data of HL-LHC and ILC 500-top respectively.

The Higgs/EW precision data at $\sqrt{s} = 250$ GeV are sensitive to the top electro-weak couplings through loop effects. The complete set of relations is found in [Table 11](#). The Higgs decay widths $\Gamma(h \rightarrow \gamma\gamma)$ and $\Gamma(h \rightarrow Z\gamma)$ are particularly sensitive to the dipole operator coefficients c_{tW} and c_{tB} that affect the $Zt\bar{t}$ and $\gamma t\bar{t}$ vertices and to the top-quark Yukawa coupling and hence C_{tH} . [Figure 3](#) and [6](#) show that the ILC precision can measure these widths to $\mathcal{O}(1)\%$ precision. In [Fig. 7](#) the individual bounds from Higgs measurements are indicated as the second, orange bar. The indirect bounds from Higgs observables are indeed found to be quite powerful for a number of operators. The individual bounds on c_{Ht} , c_{tH} and, especially c_{tB} are expected to improve the bounds from the HL-LHC measurements by one to two orders of magnitude.

Also the electro-weak precision measurements, indicated with the first, red bar in [Fig. 7](#), offer very good sensitivity. Renormalization-group mixing leads to a dependence of the electro-weak precision observables on top operators. Most individual bounds on top operator coefficients exceed the S2 projection for the HL-LHC, and in several cases ($c_{Hq}^{(3)}$, c_{Ht} , c_{tB}) by more than two orders of magnitude. In some cases, these individual bounds are competitive even when compared to the limits from direct $e^+e^- \rightarrow t\bar{t}$ production in the 500 GeV run.

The Higgs and electro-weak measurements at $\sqrt{s} = 250$ GeV therefore provide a powerful indirect handle on the top electro-weak couplings and can improve the legacy bounds from the LHC top physics programme. If these couplings receive corrections

from new physics, the Higgs/EW measurements may well be the first place where significant deviations from the SM show up. We find, however, that these individual bounds are generally not robust and an unambiguous determination of the coefficients in a global fit requires the inclusion of $e^+e^- \rightarrow t\bar{t}$ data at higher energy. The bound on the dipole operator c_{tB} is the only case, where the addition of the Higgs/EW data improves the global limit over the result of a fit to HL-LHC top physics data. For this operator a weak sensitivity of rare associated production processes ($pp \rightarrow t\bar{t}\gamma$, $pp \rightarrow t\bar{t}Z$, $pp \rightarrow tZq$) at the HL-LHC coincides with a relatively strong sensitivity of the Higgs/EW observables.

5.8 The top-quark Yukawa coupling

The top-quark Yukawa coupling is an important parameter of the SM and merits a dedicated discussion.

The indirect sensitivity to c_{tH} stems from loop-induced Higgs boson decay widths $\Gamma(h \rightarrow \gamma\gamma)$, $\Gamma(h \rightarrow Z\gamma)$ and $\Gamma(h \rightarrow gg)$ that involve top-quark loops. No other observables in [Table 11](#) depend on c_{tH} . In [Fig. 7](#) the indirect bound on c_{tH} from the ILC Higgs data is much more stringent than the direct measurement in $pp \rightarrow t\bar{t}H$ at the HL-LHC. This finding confirms the good indirect sensitivity to the Yukawa coupling found by [Ref. \[37\]](#).

However, as for the other top operators, the excellent individual bounds do not translate into a robust measurement of the top-quark Yukawa coupling. The top-quark Yukawa contributions to the Higgs decay widths are entangled with other contributions. The degeneracy between the different operator coefficients cannot be lifted with Higgs and electro-weak data alone. Indeed, the global bound on the top Yukawa in a model-independent fit is entirely dominated by the direct measurements in $t\bar{t}H$ production.

Before proceeding to discuss the direct measurements, we explore possible improvements in the indirect constraints on top Yukawa. First, $\Gamma(h \rightarrow gg)$ was identified as the most promising indirect constraint in [Ref. \[37\]](#). In addition to c_{tH} , $\Gamma(h \rightarrow gg)$ receives contributions from c_{tG} and hgg contact operators. Although the former is likely well constrained by the measurements of the top quark pair production cross section at hadron colliders with a global limit $-0.4 < c_{tG}/\Lambda^2 < 0.4$ [\[14\]](#), the degeneracy with the hgg operator is very hard to lift [\[54\]](#). On the other hand, for $\Gamma(h \rightarrow \gamma\gamma)$ and $\Gamma(h \rightarrow Z\gamma)$, c_{tH} must be separated from $c_{tW,tB}$ as well as $c_{WB,BB}$. These operators can perhaps be better constrained if differential analyses of $t\bar{t}X$ production at the LHC can improve the bounds significantly over the precision envisaged S2 scenario.

The direct measurements of the top quark Yukawa coupling have been discussed in some detail in [Ref. \[36\]](#). The HL-LHC measurements of the $t\bar{t}H$ cross section yield

a precision of 3.29% in our fit¹⁰. The precision can be further improved with $t\bar{t}h$ measurements from ILC runs at high energy. The ILC must be operated at $\sqrt{s} = 550$ GeV to match the 3% precision of the HL-LHC in the direct extraction from the $e^+e^- \rightarrow t\bar{t}h$ channel and confirm a possible deviation from the SM. The operation of a linear collider at 1 TeV can improve the constraint by another factor two. The analysis in Ref. [15] shows that the extraction from the $t\bar{t}h$ rate at the ILC is robust when data at 1 TeV are added to constrain the coefficients of $e^+e^-t\bar{t}$ operators in a global fit. The combination of all these measurements will allow to measure top-quark Yukawa coupling with approximately 1% precision.

Finally, we note an interesting direction to constrain c_{tH} . The operator RG mixes with c_6 . But we did not need to include the running of c_6 because c_6 enters in only one observable $\sigma(Zhh)$ at $\sqrt{s} = 500$ GeV. If finite loop corrections of c_6 to $\sigma(Zh)$ at $\sqrt{s} = 250$ GeV [34] can be considered in the future, multiple energy scales may yield a new way to constrain the c_{tH} 's RG contributions. The HL-LHC Higgs pair production [50] may even be used too. A more dedicated study is postponed to a future work [56].

In summary, we confirm the good indirect sensitivity of the 250 GeV run to the top-quark Yukawa coupling that was signalled by Ref. [37]. The ILC Higgs programme at 250 GeV can provide individual, single-parameter bounds on c_{tH} that are more stringent than those from the HL-LHC. Hence, the ILC initial stage may observe strong deviations from the Standard Model predictions in the $H \rightarrow \gamma\gamma$ and $H \rightarrow gg$ decay rates, should the top-quark Yukawa coupling be affected by physics beyond the Standard Model. However, we find that the indirect extraction of c_{tH} from the Higgs branching ratios is not robust in a global fit. This means that a deviation from the SM cannot unambiguously be attributed to c_{tH} ; the effect could be caused by another operator. To pinpoint the new physics effect, a measurement of the associated production rate of a Higgs boson with a top quark pair at higher energy remains necessary.

6 Summary

In this paper, we have presented a global SMEFT fit for the ILC by combining contributions from Higgs/EW and top sectors. In addition to the 22 parameters of Higgs operators and SM parameters which are complete at the lowest order [19, 51], this

¹⁰We note here that, while the extraction of the top Yukawa coupling from the $t\bar{t}h$ cross section is the most robust handle on this coupling, it is by no means immune to degradation due to the presence of other operators, as demonstrated by recent global fits [14]. Also the claim of Ref. [55] of a 1% precision on the Yukawa coupling from the ratio of the $t\bar{t}H$ and $t\bar{t}Z$ rates must be carefully assessed in a global environment.

requires seven top-quark operators. They contribute to the Higgs/EW precision observables at the one-loop suppressed order compared to those of Higgs operators (except for tree-level shifts of $t\bar{t}h$ and $t\bar{t}Z$ couplings), but they are leading contributions of top operators. The 29-parameter fit then provides a complete and model-independent description of leading Higgs+EW+top effects on precision observables at future lepton colliders.

The loop calculations of top effects necessarily introduce new uncertainties. The top-loop contributions were included through the renormalization mixing with Higgs operators. Although good proxies of full one-loop effects, the RG contributions are only a subset of the full one-loop results¹¹. The impact of RG effects depend on the renormalization scale Q to which the Higgs operators will run from a common scale Q_0 where all the operators are defined. $Q = \max(m_t, Q_{\text{proc}})$ was used as the default choice, but the variations with respect to $Q = Q_{\text{proc}}$ and $\max(2m_t, Q_{\text{proc}})$ reflect the errors from even higher-order quantum corrections.

With this formalism, we have evaluated the prospects of the ILC in the extended 29-parameter basis, in comparison with those of the previous 22-parameter fit of Ref. [1]. We have found that the Higgs fit at ILC 250 GeV is strongly affected by the inclusion of top effects. This result, and those of Ref. [2, 3], show that results obtained with today’s state of the art SMEFT fits must be interpreted with care, as they may not hold in a more complete fit¹².

To mitigate the effect of the additional degrees of freedom, their contribution must be disentangled by including precise measurements of the top quark electro-weak couplings. The precision of the HL-LHC top physics program, as envisaged in the S2 scenario of Ref. [15], is sufficient to restore the precision of the physical Higgs boson couplings. But it still leaves several of the underlying EFT operator coefficients relatively poorly constrained. This implies that, even if the Higgs couplings can be precisely determined and their deviations from SM predictions can be well detected, it becomes harder to pinpoint the source of the deviations, should they be observed. The projection of the EFT fit results on the physical Higgs couplings offers a set of bounds with an intuitive *physical* interpretation, but can obscure potentially very important

¹¹ While including full one-loop effects for all the relevant observables is beyond the scope of this paper, we recognize that the important effect from the left-over finite contributions would be mainly coming from c_{tB} term in $\Gamma(h \rightarrow \gamma\gamma)$, provided the prospected constraints on top operators from HL-LHC; see details in Appendix B.2.

¹²As a familiar example, one can consider the well-known κ -framework to interpret Higgs boson coupling measurements. Clearly, the limitations of the κ framework affect the conclusions of a benchmark analysis in important ways: due to the assumptions inherent in the fit, it fails to acknowledge the role of EWPO and beam polarization, to name just two examples. The importance of these aspects becomes apparent only in a more advanced EFT approach.

information. It is therefore important to present both sets of results – Higgs coupling precisions and operator constraints – to fully characterize the analyzing power of the data.

We also assess whether the Higgs/EW precision data in the initial stage at $\sqrt{s} = 250$ GeV can place bounds on top operators before top quark pairs are produced at the ILC. These indirect bounds are very very competitive if only a single top operator is considered in a fit. For example, the $h \rightarrow gg$ and $h \rightarrow \gamma\gamma$ decay rates yield indirect sensitivity on the top coupling at sub-% precision, well beyond what can be achieved in associated $t\bar{t}h$ productions in all planned lepton or hadron colliders. However, these individual bounds turn out to be not robust in the presence of other operators with non-zero coefficients. A robust determination of top operators requires the inclusion of $e^+e^- \rightarrow t\bar{t}$ and $e^+e^- \rightarrow t\bar{t}h$ data at higher center-of-mass energy.

In the complete ILC programme, with a second energy stage at 500 GeV, a precise characterization of the $e^+e^- \rightarrow t\bar{t}$ process provides very precise constraints on the top operators. A combined fit on Higgs, EW and top quark precision data then over-constrains the EFT fit, yielding robust bounds on all 29 operators and the unambiguous identification of the origin of any deviations from the SM.

Acknowledgments

This work builds on the effort of the LHC collaborations and the ILC and CLIC simulation studies. We would like to acknowledge the work of our colleagues in this place. We owe special thanks to Gauthier Durieux, Michael Peskin and Cen Zhang for their feedback on the project and write-up. SJ and JL are supported by Grant Korea NRF-2019R1C1C1010050, 2017R1D1A1B03030820, 2015R1A4A1042542, and SJ also by POSCO Science Fellowship. MP and MV are supported by the Spanish national program for particle physics, projects FPA2015-65652-C4-3-R (MINECO/FEDER) and PGC2018-094856-B-100, and PROMETEO grant 2018/060 of the Generalitat Valenciana. MP is supported by the Severo Ochoa Grant SEV-2014-0398-05, reference BES-2015-072974. JT was supported by the Japan Society for the Promotion of Science (JSPS) under Grants-in-Aid for Science Research 15H02083.

A Typos and corrections in Ref.[1]

Ref. [1, 19] and the distributed C++ code, on which our study is based, contain several mild typos and mistakes. We collect them in this appendix using the same notation, and we make the corrected Mathematica code available upon request.

1. Typos in the paper [1]:

- (a) Some expressions for the TGCs written in the Section 3 and Appendix of Ref. [1] should be corrected in a right form. The amplitudes of $e_{R,L}^- e_{L,R}^+ \rightarrow W_L^+ W_L^-$ are

$$\mathcal{A}_R = e^2 \kappa_A - g_R g_Z \kappa_Z, \quad (\text{A.1})$$

$$\mathcal{A}_L = e^2 \kappa_A - g_L g_Z \kappa_Z - \frac{g_W^2}{2}. \quad (\text{A.2})$$

The κ_V denote the deviation of the triple gauge couplings between $W^+ W^-$ and $V (= Z, A)$. The g_W is the W boson coupling to leptons (electron and neutrino) that is introduced only to the amplitude for $e_L^- e_R^+$ through the neutrino exchange diagram. In the Ref. [1], the sign of the terms for $g_L (g_R) g_Z \kappa_Z$ is written as plus but the negative one is correct. The fits were done with the correct sign but one term for δe in $\delta g_{Z,eff}$ was missed. By the definition of the effective TGC ([1]),

$$\delta g_{Z,eff} = \frac{1}{g c_w^2} (2\Delta \mathcal{A}_L - \Delta \mathcal{A}_R), \quad (\text{A.3})$$

the $\delta g_{Z,eff}$ has one more term which was missed and we find

$$\delta g_{Z,eff} = \delta g_Z + \frac{1}{c_w^2} ((c_w^2 - s_w^2) \delta g_L + s_w^2 \delta g_R - 2\delta g_W + 2s_w^2 \delta e). \quad (\text{A.4})$$

This can be checked using the fact that the TGCs are independent of $c_{WB, BB, WW}$ because the $\Delta \mathcal{A}_{R,L}$ are also independent of them.

2. Typos in the code distributed with [1]:

- (a) $\delta g_R = -c_w^2 \delta g + (1 + c_w^2) \delta g' - \frac{1}{2s_w^2} c_{HE} - \frac{1}{2} c_w^2 (8c_{WW}) + c_w^2 (8c_{WB}) + \frac{1}{2} \frac{s_w^2}{c_w^2} (1 + c_w^2) (8c_{BB})$: the sign of the $(8c_{WW})$ was reversed.
- (b) $b_L = \frac{1}{(1-2s_w^2)} \left[c_w^2 (1 - 2s_w^2 \frac{m_Z^2}{s}) (8c_{WW}) + 2s_w^2 (1 - 2s_w^2) \frac{m_Z^2}{s} (8c_{WB}) - \frac{s_w^4}{c_w^2} (1 - 2c_w^2 \frac{m_Z^2}{s}) (8c_{BB}) \right]$
: $-\frac{1}{c_w^2} (1 - 2c_w^2 \frac{m_Z^2}{s}) (8c_{BB})$ was used instead of the above $(8c_{BB})$ term.

- (c) $k_h = -\frac{E_Z m_h^2}{2k^2 \sqrt{s}} - \frac{E_Z^2/m_Z^2}{(2+E_Z^2/m_Z^2)} \frac{m_h^2}{E_Z \sqrt{s}}$ in the Zh measurement.
: the first term was inserted as $-\frac{E_Z m_Z^2}{2k^2 \sqrt{s}}$. The Z boson mass was used for the Higgs mass.
- (d) $\delta\sigma(R) = 2\delta g_R + 1.40\eta_Z + 1.02\eta_{ZZ} + 18.6\delta Z_Z - 28.7\delta Z_{AZ} + 0.56\eta_h + \dots$ for the Zhh cross section.
: $2\delta g_L$ was used instead of the first term, $2\delta g_R$ in the estimate of the uncertainty of $\sigma(Zhh)$.
- (e) In the fits for “+Zh” columns in [Table 5](#), the a_L, a_R parameters were inserted in the place of b_L, b_R as error inputs of the Zh measurement but in ILC 250,500 fits the error inputs were used correctly.
- (f) When the total cross section of $e^-e^+ \rightarrow Zh$ is prepared for the its error estimate in the fits for 250+350 GeV in the fourth column of [Table 6](#), only left-handed one was inserted, that is right-handed one was missing.

By correcting the typos, we re-obtain the Table 2 in Ref. [\[1\]](#) and Table 3 in [\[19\]](#) in [Table 5](#) and [6](#), respectively. The impact of the typos on the Higgs precision is rather mild while the impact on some operators is significant. Especially, the constraint on c_{HE} decreases significantly from the “+LHC” column as shown in [Table 5](#) mainly due to [item 2a](#) and the difference reduces at the ILC 500 and ILC 250+500 fits where the influence of the LHC Higgs measurements becomes weak relatively. We also found that the missing right-handed $\sigma(Zh)$ part ([item 2f](#)) in the 250+350 GeV fit reduces the error of the cross section to the half of the original value as shown in the “+1.5/ab 350 GeV” column of [Table 6](#).

	prec. EW		+ WW		+ LHC		+ Zh		ILC 250	
	rep.	corr.	rep.	corr.	rep.	corr.	rep.	corr.	rep.	corr.
c_T	0.011	0.011	0.051	0.051	0.051	0.051	0.048	0.049	0.052	0.050
c_{HE}	0.043	0.043	0.026	0.026	0.085	0.026	0.047	0.024	0.055	0.025
c_{HL}	0.042	0.042	0.035	0.035	0.035	0.035	0.032	0.03	0.039	0.030
c'_{HL}	.	.	0.028	0.028	0.028	0.028	0.028	0.027	0.047	0.039
$8c_{WB}$.	.	0.078	0.078	0.080	0.080	0.076	0.078	0.090	0.091
$8c_{BB}$	0.20	0.20	0.16	0.18	0.11	0.17
$8c_{WW}$	0.21	0.21	0.13	0.17	0.13	0.19
$8c_H$	1.12	1.12	1.20	0.99

	prec. EW		+ WW		+ LHC		+ Zh		ILC 500		ILC 250+500	
	rep.	corr.	rep.	corr.	rep.	corr.	rep.	corr.	rep.	corr.	rep.	corr.
c_T	0.011	0.011	0.046	0.046	0.047	0.047	0.041	0.041	0.037	0.041	0.030	0.036
c_{HE}	0.043	0.043	0.015	0.015	0.077	0.015	0.040	0.014	0.01	0.01	0.009	0.008
c_{HL}	0.042	0.042	0.030	0.030	0.030	0.030	0.027	0.018	0.016	0.015	0.013	0.012
c'_{HL}	.	.	0.027	0.027	0.028	0.028	0.026	0.018	0.014	0.015	0.011	0.012
$8c_{WB}$.	.	0.070	0.070	0.072	0.071	0.067	0.066	0.052	0.069	0.041	0.059
$8c_{BB}$	0.20	0.20	0.15	0.16	0.088	0.16	0.062	0.12
$8c_{WW}$	0.21	0.21	0.11	0.14	0.044	0.14	0.039	0.10
$8c_H$	4.8	2.2	1.2	1.2	0.65	0.68

Table 5. The corrected 1σ constraints on the EFT coefficients in %, which can be compared with Table 2 of Ref.[1]. The “rep.” columns present the numbers we reproduce for the results of [1] with typos; they are same. The “corr.” columns give the corrected results.

	2/ab w. pol.		2/ab 350 GeV		5/ab no. pol.		+ 1.5/ab 350 GeV		full ILC	
	rep.	corr.	rep.	corr.	rep.	corr.	rep.	corr.	rep.	corr.
$g(hb\bar{b})$	1.04	0.98	1.08	1.04	0.98	0.92	0.66	0.66	0.55	0.56
$g(hc\bar{c})$	1.79	1.75	2.27	2.25	1.42	1.38	1.15	1.15	1.09	1.10
$g(hgg)$	1.60	1.56	1.65	1.63	1.31	1.26	0.99	0.99	0.89	0.90
$g(hWW)$	0.65	0.54	0.56	0.50	0.80	0.73	0.42	0.42	0.34	0.36
$g(h\tau\bar{\tau})$	1.17	1.11	1.35	1.31	1.06	1.00	0.75	0.75	0.71	0.73
$g(hZZ)$	0.66	0.55	0.57	0.51	0.80	0.73	0.42	0.42	0.34	0.37
$g(h\gamma\gamma)$	1.21	1.12	1.15	1.11	1.26	1.19	1.04	1.04	1.01	1.01
$g(h\mu\mu)$	5.53	5.51	5.71	5.70	5.10	5.08	4.87	4.87	4.95	4.95
$g(hb\bar{b})/g(hWW)$	0.82	0.82	0.90	0.90	0.58	0.58	0.51	0.51	0.43	0.43
$g(hWW)/g(hZZ)$	0.07	0.07	0.06	0.07	0.07	0.07	0.06	0.07	0.05	0.06
Γ_h	2.38	2.25	2.50	2.38	2.11	2.01	1.49	1.49	1.50	1.54
$\sigma(e^-e^+ \rightarrow Zh)$	0.70	0.70	0.77	0.75	0.50	0.49	0.22	0.44	0.61	0.61
$BR(h \rightarrow inv)$	0.30	0.30	0.56	0.56	0.30	0.30	0.27	0.27	0.28	0.28
$BR(h \rightarrow other)$	1.50	1.51	1.63	1.60	1.09	1.09	0.94	0.94	1.15	1.16

Table 6. The corrected Higgs coupling precision in %, which can be compared with Table 3 of Ref.[19]. The “rep.” columns present the numbers we reproduce for the results of [1] with typos; they are same. The “corr.” columns give the corrected results.

B Comparison with Ref.[2, 3]

Both our work and Ref. [2, 3] perform global-fit analyses for the combined Higgs, EW and top precision at future electron-positron colliders. They have notable differences, which are discussed and compared in this appendix.

Above all, we focus on the projection of linear lepton colliders (using ILC inputs) while [2, 3] on circular colliders; some of the linear versus circular colliders are also presented in Section 5.3. In addition to well-known differences of linear versus circular colliders, we use upgraded direct-top constraints from the 10-parameter fit at the HL-LHC S2 stage [15], which yields $\mathcal{O}(1)$ -factor stronger constraints on top operators than the HL-LHC inputs used in [2, 3]. The upgraded results were not yet available at the time Durieux et al. performed their study.

In the rest of this appendix, starting from different operator choices and assumptions, we discuss important differences in computing the contributions of top operators.

B.1 Operator choice

Although a quite general set of Higgs and top operators were used in both works, different assumptions were made to reduce the number of independent operators in global-fit analyses. They do not induce significant differences in numerical results, but it is worth collecting them here.

On Higgs operators, Ref. [2, 3] insisted the universality of the theory and perfect EWPO, while we do not. For the universality introduced in [31], they replaced the light fermion operators like $\mathcal{O}_{HE,HL}$ and \mathcal{O}'_{HL} with \mathcal{O}_W and \mathcal{O}_B using equations of motion. In addition, for the perfect EWPO, they fixed the values of $c_{HWB,HD}$ required to make the oblique parameters, S and T , vanish. These Wilson coefficients are replaced by top operator contributions to adjust the oblique parameters to be zero. However, we include $c_{HE,HL,HL'}$ and our counterparts of $c_{HWB,HD}$ ($c_{WB,T}$ as in Eq. (E.3)) and let them vary freely in the global fit by including the EWPO data.

As for top operators, Ref. [2, 3] removed one combination of $\mathcal{O}_{Hq}^{(1)}$ and $\mathcal{O}_{Hq}^{(3)}$ by assuming that the measurement of the $Z\bar{b}b$ coupling is perfect. Moreover, they ignored \mathcal{O}_{Htb} since its contributions are suppressed by the bottom Yukawa coupling; one exception could be its contribution to \dot{c}_{bH} in Eq. (E.5), but this running is not relevant to our work. On the other hand, we have included all of them, $\mathcal{O}_{Hq}^{(1)}$, $\mathcal{O}_{Hq}^{(3)}$ and \mathcal{O}_{Htb} , as well as the $Z\bar{b}b$ measurement through the work of Ref. [15].

Another difference is on the treatment of the hgg vertex. Although they included both $\mathcal{O}_{tG} = (\bar{Q}\sigma^{\mu\nu}T^A t)\tilde{\Phi}G_{\mu\nu}^A + h.c.$ and $\mathcal{O}_{GG} = (\Phi^\dagger\Phi)G_{\mu\nu}^A G^{A\mu\nu}$ which contribute to the hgg vertex, we use c_{gH} to describe all those effects collectively as the hgg contact interaction, as discussed in Section 3.1 and in Ref. [1]. \mathcal{O}_{tG} will indeed be well con-

strained by LHC $t\bar{t}$ measurements, as was also assumed in [15] from which we take our direct-top data; see also Section 5.8.

B.2 Finite versus log effects of top quarks

Another important difference is the way to compute the contributions of top operators. Our work accounts for the logarithmic terms of top-loop effects, computed by the RG evolutions of Higgs operators. Ref. [2, 3] computed one-loop diagrams by top operators instead, which then includes log-terms (captured also in our RG calculation) as well as non-log finite terms of the loop diagrams. On the other hand, our power counting rule allows us to include two-loop top effects in $\delta\Gamma(h \rightarrow \gamma\gamma, Z\gamma)$ (see Section 3.4) which were not added in [2, 3]. We assess the numerical impact of finite terms and higher-order terms in Appendix B.2 and B.3, respectively.

The log and finite terms of top-loop effects on several Higgs observables can be extracted from Table 14 of [3]. The finite terms are obtained from the results with RG scale $\mu_{\text{EFT}} = m_h$, where all log terms with $\log \mu_{\text{EFT}}/m_h$ vanish. The log terms then can be obtained from the subtraction of two results with $\mu_{\text{EFT}} = m_h$ and 1 TeV since finite terms are independent on the RG scales. The extracted results are tabulated in the second and third lines in Table 7.

Also listed in the Table are our results of log terms. For the comparison, our calculation must be corrected to account for on-shell mass renormalization and ignored higher-order terms. The former affects $\delta\Gamma(h \rightarrow b\bar{b}, l\bar{l})$ and the latter affects loop-induced $\delta\Gamma(h \rightarrow \gamma\gamma, Z\gamma)$ as

$$\delta\Gamma(h \rightarrow b\bar{b}) = -\frac{1}{2}c_H + 2c_{bH} + \dots, \quad (\text{B.1a})$$

$$\delta\Gamma(h \rightarrow l\bar{l}) = -\frac{1}{2}c_H + 2c_{lH} + \dots, \quad (\text{B.1b})$$

$$\delta\Gamma(h \rightarrow \gamma\gamma) = 528 \delta Z_A, \quad (\text{B.1c})$$

$$\delta\Gamma(h \rightarrow Z\gamma) = 290 \delta Z_{AZ}, \quad (\text{B.1d})$$

where \dots denotes the variation of SM parameters δv and $\delta\bar{\lambda}$, not relevant to the comparison of top contributions in this appendix. Another piece to correct is to add the running of Yukawa operators c_{bH} and c_{lH} , according to Eq. (E.5) and

$$\dot{c}_{lH} = 2N_c y_t c_H - 4N_c (y_t^2 + y_b^2) c_{Hq}^{(3)} + 4N_c y_t y_b c_{Htb}. \quad (\text{B.2})$$

The corrected log terms are shown in the first line of Table 7. Our corrected log terms and those of [3] agree well, as it should be.

channel		\mathcal{O}_{Ht}	$\mathcal{O}_{Hq}^{(1)}$	$\mathcal{O}_{Hq}^{(3)}$	\mathcal{O}_{Htb}	\mathcal{O}_{tW}	\mathcal{O}_{tB}	\mathcal{O}_{tH}
$h \rightarrow bb$	Our log(B.1)	0	0.04	1.91	-7.90	-0.62	0	0.48
	log-term([3])	0	0.04	2.08	-7.05	-0.62	0	0.47
	finite-term([3])	0	0.04	-0.18	-1.13	-0.28	0	-0.18
$h \rightarrow ll$	Our log(B.1)	0	0	0.94	-0.03	0	0	0.95
	log-term([3])	0	0	0.94	-0.03	0	0	0.95
	finite-term([3])	0	0	-0.04	-0.00	0	0	-0.27
$h \rightarrow \gamma\gamma$	Our log(B.1)	0	0	0	0	200.9	366.2	0
	log-term([3])	0	0	0	0	187.9	350.8	0
	finite-term([3])	0	0	0	0	-73.3	-136.8	3.45*
$h \rightarrow Z\gamma$	Our log(B.1)	0	0	0	0	119.3	-20.9	0
	log-term([3])	0	0	0	0	117.1	-16.7	0
	finite-term([3])	1.77*	1.80*	-1.74*	0	-45.8	6.97	0.72*

Table 7. The comparison of log versus finite terms of top-loop contributions in the deviations of the Higgs decay widths. The coefficient of each top operator contribution is shown in % with $1/(1\text{ TeV})^2$ instead of $1/v^2$ normalization. The first line “Our log” shows the RG-running contributions of Higgs operators (induced by top operators) calculated in this work and corrected as in Eq. (B.1) to be compared with [3]. The second and third lines show the log and finite terms computed in [3]. The finite terms are not added in our work. The impact of finite terms is numerically explored in Fig. 8. The starred(*) numbers are not relevant to the comparison (but shown for completeness) as they are from the tree-level shifts of $Z\bar{t}t$ and top Yukawa couplings, without log counterparts. $Q = m_h$.

Remarkably, Table 7 shows that finite terms are usually smaller than or, at most, the same order as the log terms. All non-zero entries of finite terms are also generated by log terms (the starred entries of finite terms are included in our work too, as they are generated by tree-level shift of top couplings). Thus, it is reasonable to expect that RG results are good proxies of loop effects.

Finite terms could induce $\mathcal{O}(1)$ uncertainties in our global-fit results without finite terms. Figure 8 explores this by adding all finite terms extracted in Table 7 to our analyses, albeit not full effects of finite terms. First of all, the Higgs coupling precision is worsened by $\mathcal{O}(1)$ at the ILC 250, but becomes robust against finite terms at the ILC 500. On the other hand, operator constraints are robust initially at the ILC 250 but become affected by $\mathcal{O}(1)$ at the ILC 500. Notably, adding finite terms could improve some operator constraints (while usually worsening the Higgs coupling precision). As stronger dataset become available, Higgs couplings may be better measured semi-

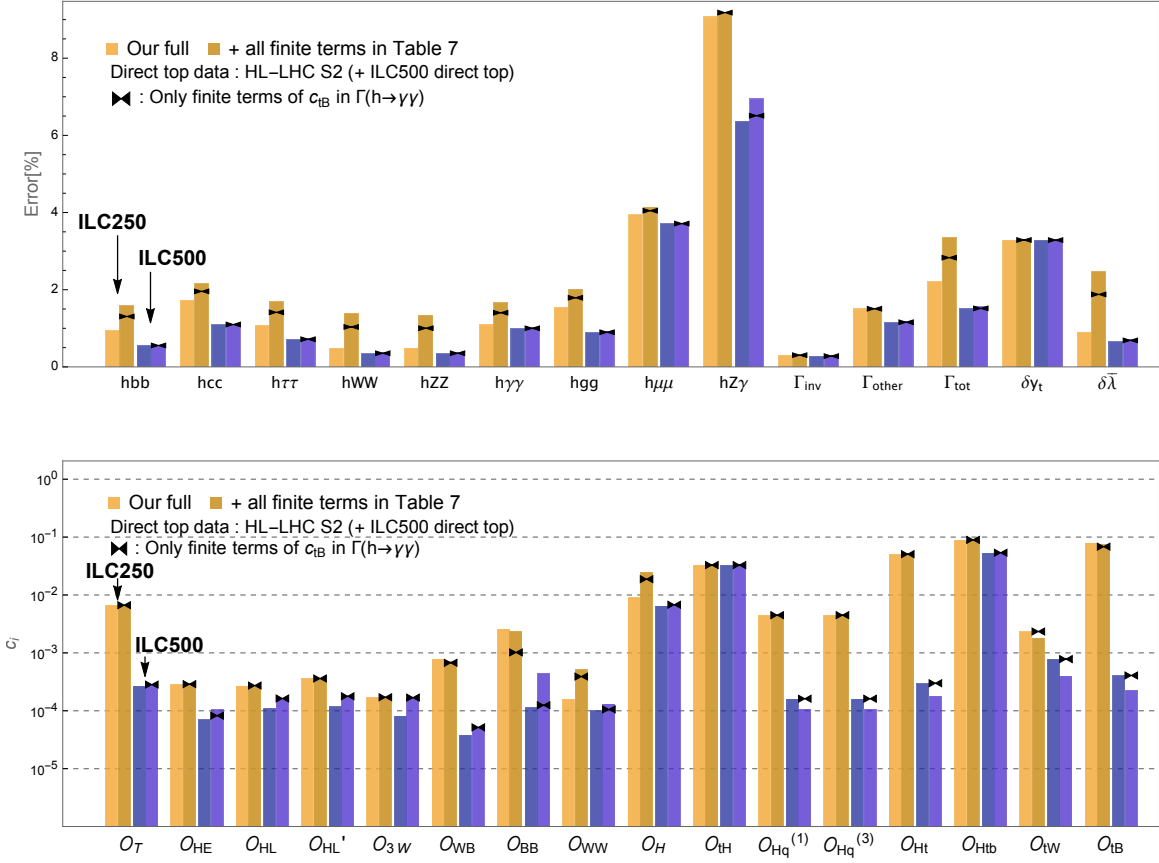


Figure 8. The effects of finite terms of top-loop diagrams on the Higgs coupling precision (upper panel) and operator constraints (lower) at the ILC 250 (yellow) and 500 stage (blue). For each case, two bars are shown: the first bar is just our full result that does not include the finite terms, while the second bar includes all the finite terms in Table 7. Also marked in the second bar is the result obtained with only finite terms proportional to c_{tB} in $\delta\Gamma(h \rightarrow \gamma\gamma)$.

directly while operator constraints may become sensitive enough to feel extra finite terms. Lastly, also marked in Fig. 8 are the results with only finite terms proportional to c_{tB} added to $\delta\Gamma(h \rightarrow \gamma\gamma)$. The c_{tB} was expected to be influential as it is relatively weakly constrained while RG-mixing strongly with $c_{WB, BB}$ (Section 5.2). Indeed, c_{tB} finite terms seem to cause major impact among finite-term effects.

B.3 Higher-order effects of top quarks

For $\delta\Gamma(h \rightarrow \gamma\gamma, Z\gamma)$, Higgs operators contribute either through the tree-level renormalization of SM expressions (hence, $c_{H,T}$ at absolute one-loop) or through the tree-level

channel		\mathcal{O}_{Ht}	$\mathcal{O}_{Hq}^{(1)}$	$\mathcal{O}_{Hq}^{(3)}$	\mathcal{O}_{Htb}	\mathcal{O}_{tW}	\mathcal{O}_{tB}	\mathcal{O}_{tH}
$h \rightarrow \gamma\gamma$	Our full	0	0	1.05	-0.03	28.07	51.24	-0.57
	Without higher-order	0	0	0	0	28.02	51.05	-0.57
$h \rightarrow Z\gamma$	Our full	-0.71	0.14	2.26	-0.07	16.62	-2.79	-0.11
	Without higher-order	-0.29	-0.29	0.29	0	16.64	-2.93	-0.11

Table 8. The higher-order (two-loop) contributions of top quarks in the loop-induced Higgs decay widths. The coefficient of each top operator contribution is shown in absolute value with $1/v^2$ normalization. Although two-loop originated, they are only one-loop suppressed compared to the SM contributions. The first line “Our full” shows the full results of this work including such higher-order effects while the second line without them. The higher-order effects were ignored in [2, 3]. The impact of higher-order effects is numerically explored in Fig. 9. $Q = \max(m_t, Q_{\text{proc}})$.

contact interaction of $h\gamma\gamma$ and $hZ\gamma$ (hence, $c_{WW,WB,BB}$ at absolute tree-level). Since those widths are one-loop induced in the SM, our power counting insists on including absolute two-loop top-quark corrections. On the other hand, Ref. [2, 3] considered only absolute one-loop top corrections. To estimate their impact, the higher-order terms of top operators are extracted from our calculation and tabulated in Table 8.

Table 8 shows that largest higher-order effects come from $c_{Ht,Hq1,Hq3}$ which renormalize c_H and c_T . Although these two-loop effects are smaller than the one-loop effects of $c_{tW,tB}$ renormalizing the tree-level contact interactions induced by $c_{WW,WB,BB}$ ¹³, these $\mathcal{O}(0.1-1)$ terms are not small compared to most entries of top contributions in Table 11 (actually larger than most entries). This is consistent with an underlying logic of our power counting rule that the relative order matters. Moreover, higher-order effects can be leading contributions, e.g. for $\mathcal{O}_{Hq}^{(3)}$ and \mathcal{O}_{Htb} in $\delta\Gamma(h \rightarrow \gamma\gamma, Z\gamma)$.

Figure 9 shows the impact of higher-order terms by comparing the global-fit results with and without higher-order terms in Table 8. The results with higher-order terms are our full global-fit results. Compared to Fig. 8, higher-order effects are somewhat smaller in general (Higgs coupling precision in particular), partly because only two observables are modified by higher-order effects. But still, as stronger dataset becomes available, $g(hZ\gamma)$ precision and several operator constraints become sensitive to higher-order terms and change by $\mathcal{O}(1)$.

¹³Small higher-order effects proportional to $c_{tW,tB}$ are from the renormalization of SM parameters such as δe and δm_W . As an aside, c_{Htb} terms are small proportional to y_b , and \mathcal{O}_{tH} does not RG mix in our work.

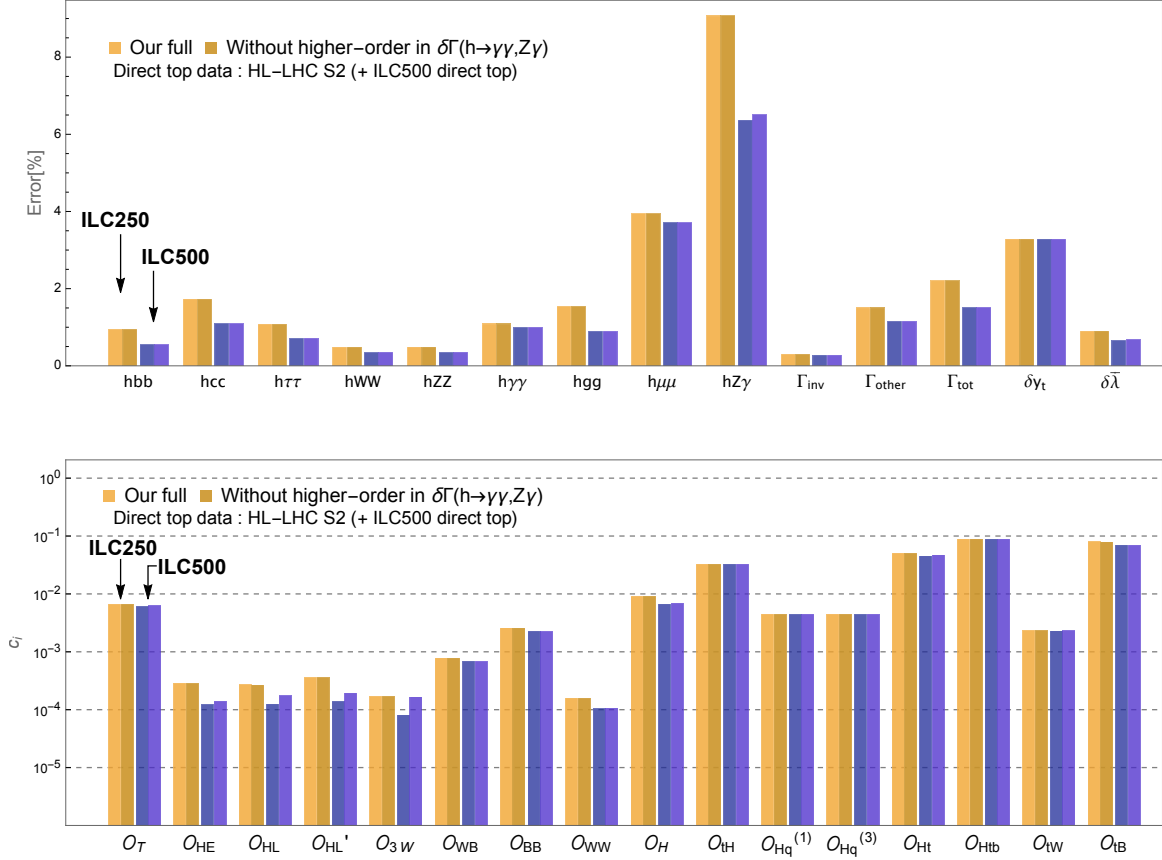


Figure 9. The effects of higher-order (two-loop) top contributions on the Higgs coupling precision (upper panel) and operator constraints (lower) at the ILC 250 (yellow) and 500 stage (blue). For each case, two bars are shown: the first bar is just our full result that includes the higher-order terms, while the second bar does not. Such top contributions are tabulated in [Table 8](#).

C Results with different renormalization scale Q

Loop calculations necessarily involve the uncertainty due to the choice of the RG scale Q . We have chosen $Q = \max(m_t, Q_{\text{proc}})$ in the main text, but also introduced other choices $Q = \max(2m_t, Q_{\text{proc}})$ and $Q = Q_{\text{proc}}$ in Section 3.5. In Fig. 10, we compare global-fit results with those three choices of Q .

First of all, the variations of the Higgs coupling precision and operator constraints are $\sim \mathcal{O}(10\%)$ at the ILC 250 with LHC Run 2. But stronger direct-top constraints from HL-LHC S2 make this variation from top effects smaller. One can expect that at the ILC 500, even though there will be more multiple scales, stronger direct-top data may not significantly increase the variation. These are the uncertainties in our results due to the choice of Q . In principle, this size of uncertainty is inevitable in perturbative calculations which can only be reduced by carrying out even higher-order calculations.

More interestingly, Higgs coupling precision is most robust against the addition of top-quark effects when $Q = \max(2m_t, Q_{\text{proc}})$ is used. This is already discussed in Section 5.2 as the main reason why Higgs coupling precision at the ILC can be robust against top effects; the more number of common scales in the fit observables, the better can Higgs couplings be semi-directly measured.

On the other hand, the very many common scales may harm operator constraints since top RG effects can only be discerned from multiple energy scales. Figure 10 indeed shows that operator constraints vary somewhat more than Higgs coupling precision. But notably, operator constraints also become most robust when $Q = \max(2m_t, Q_{\text{proc}})$, which provides more numbers of common energy scales $2m_t$ so that RG effects are expected to be harder to discern. This is partly because $2m_t$ is closer to $Q_0 = 1$ TeV from which we RG evolve operators, so that RG effects with $Q = \max(2m_t, Q_{\text{proc}})$ are smaller than with other choices of Q .

Lastly, Fig. 11 (compared with Fig. 4) shows that the beam polarization becomes more important with $Q = Q_{\text{proc}}$ than with other choices. As discussed in Section 5.3, it is because more various energy scales are involved so that the beam polarization can efficiently double the number of independent observables, disentangling the Higgs and top operators. Also, finite terms and higher-order effects may not be described by a small number of \tilde{c}_i combinations (introduced in Section 5.2), which then make the beam polarization more useful.

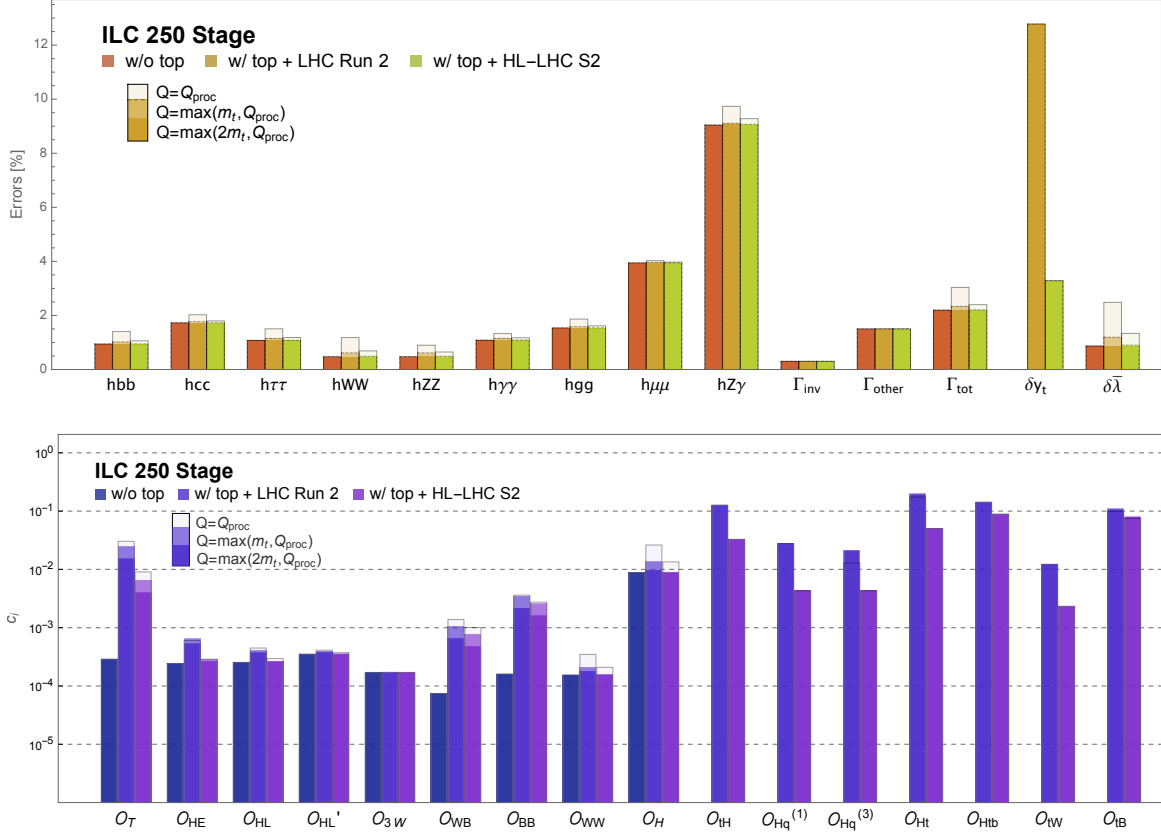


Figure 10. Global-fit results with various choice of $Q = Q_{\text{proc}}, \max(m_t, Q_{\text{proc}})$ and $\max(2m_t, Q_{\text{proc}})$ at the ILC 250 stage.

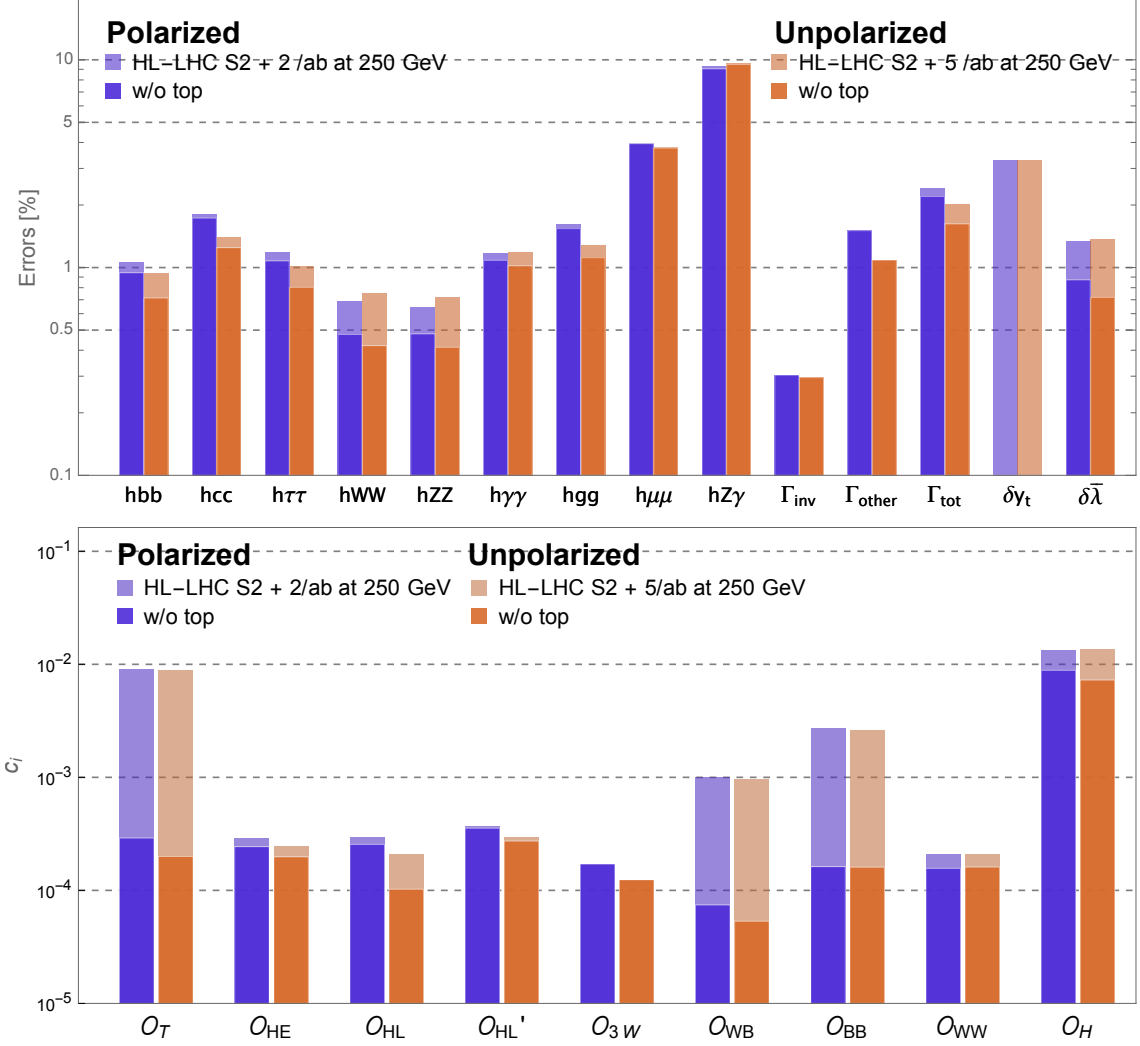


Figure 11. Same as Fig. 4 but with $Q = Q_{proc}$. Not only the variations due to top effects become larger, but also the impact of beam polarization becomes more visible.

D The Q_0 scale dependence

As introduced in Section 3.5, the Q_0 is a reference scale (different from the RG scale Q) at which we renormalize operators and express their constraints. This is arbitrary in the viewpoint of numerical analyses although this can be related to the new physics scale or the matching scale of the SMEFT. Numerically, our final results must not depend on the choice of Q_0 ; unlike the case of Q , no inevitable numerical uncertainties are generated. This must imply one property of the covariance matrix: it should change with Q_0 in such a way to compensate the RG evolutions of Higgs operators. We detail this in Appendix D.1 and D.2, and apply this to understand the connection of $c_T(Q_0)$ and oblique parameters in Appendix D.3.

D.1 The running of the covariance matrix

The measurements involved in our global fits are performed at various energy scales. Theory predictions are written in terms of the Wilson coefficients renormalized at Q_0 . The fit results then represent the constraints on the operator coefficients at Q_0 . If we change the Q_0 to Q'_0 , the constraints change as shown in Fig. 12.

As discussed in Section 5.1, the covariance matrix $\mathcal{Cov}_{IJ}(Q_0)$ encodes the RG evolutions of operators from Q_0 to the RG scales of observables. It also changes with Q_0 in such a way to leave the total χ^2 of the global fit unchanged

$$\chi^2 = \sum_{I,J} c_I(Q_0) \mathcal{Cov}_{IJ}^{-1}(Q_0) c_J(Q_0) = \sum_{I,J} c_I(Q'_0) \mathcal{Cov}_{IJ}^{-1}(Q'_0) c_J(Q'_0). \quad (\text{D.1})$$

The Wilson coefficients $c_I(Q_0)$ RG evolve as

$$c_I(Q'_0) = \begin{pmatrix} c_i(Q'_0) \\ c_j(Q'_0) \end{pmatrix} = \begin{pmatrix} 1_{ii'} & \gamma_{ij'} \log(Q'_0/Q_0) \\ 0 & 1_{jj'} \end{pmatrix} \begin{pmatrix} c_{i'}(Q_0) \\ c_{j'}(Q_0) \end{pmatrix} \equiv \Gamma_{IJ}(Q'_0/Q_0) c_J(Q_0), \quad (\text{D.2})$$

where the upper(lower) components $c_i(c_j)$ denote the coefficients of Higgs(top) operators and I, J denote the indices i, j collectively. The block diagonal form of Γ_{IJ} is from our scheme where only the RG evolutions of Higgs operators by top operators are considered. Thus, the covariance matrix must evolve as

$$\mathcal{Cov}(Q'_0) = \Gamma(Q'_0/Q_0) \mathcal{Cov}(Q_0) \Gamma(Q'_0/Q_0)^T. \quad (\text{D.3})$$

Again, this evolution ensures that global-fit results obtained with different Q_0 are physically equivalent (same χ^2), and one result can be obtained from the other through the evolution of the covariance matrix.

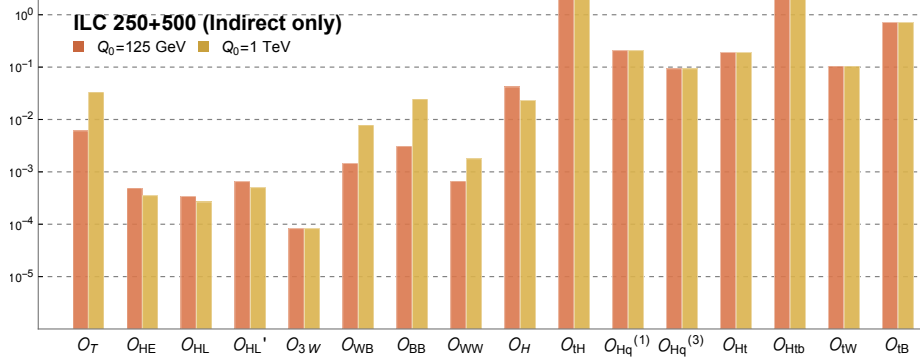


Figure 12. The comparison of global fits performed with $Q_0 = m_h$ and 1 TeV. The two result are equivalent because one of them can be obtained by the other via the RG evolution of the covariance matrix. It also shows that \mathcal{O}_T runs most quickly due to top operators.

As an aside, we mention properties of the evolution of covariance matrix. Note that $\Gamma^{-1}(Q/Q') = \Gamma(Q'/Q)$ and $\Gamma(Q''/Q')\Gamma(Q'/Q) = \Gamma(Q''/Q)$ make the evolution similar to (RG-)logarithmic. The diagonal component of the covariance matrix \mathcal{Cov}_{II} is an error of a corresponding Wilson coefficient, and the off-diagonal element \mathcal{Cov}_{IJ} is the error correlation between c_I and c_J . These components evolve as

$$\begin{aligned} \mathcal{Cov}_{II}(Q'_0) &= \mathcal{Cov}_{II}(Q_0) + \sum_J 2\gamma_{IJ} \log(Q'_0/Q_0) \mathcal{Cov}_{IJ}(Q_0) \\ &+ \sum_J (\gamma_{IJ} \log(Q'_0/Q_0))^2 \mathcal{Cov}_{JJ}(Q_0). \end{aligned} \quad (\text{D.4})$$

For coefficients that do not RG evolve by top operators, the equation reduces to $\mathcal{Cov}_{II}(Q_0) = \mathcal{Cov}_{II}(Q'_0)$. Thus their constraints do not change with Q_0 . Examples include the constraints on top operators and c_{3W} as shown in Fig. 12.

D.2 The Q_0 independence of the uncertainty of observables

The evolution of the covariance matrix also ensures that the (physical) results defined at certain Q_{proc} (such as Higgs coupling precision and oblique parameters) are independent on Q_0 . Start from the theory prediction of the deviations of the observable $\delta\mathcal{O}$ defined at Q

$$\delta\mathcal{O}(Q) = \sum_I a_I(Q) c_I(Q) = \sum_{I,J} a_I(Q) \Gamma_{IJ}(Q/Q_0) c_J(Q_0) = \sum_J a_J(Q_0) c_J(Q_0), \quad (\text{D.5})$$

where a_I is the constant multiplied in front of each Wilson coefficient c_I , i.e. numbers collected in Table 10 and 11. This determines the rule for the transformation of a_I

	αS	αT
ILC 250+500 without top operators	0.0189 %	0.0175 %
With top operators (indirect-only)	0.0268 %	0.0177 %
+ HL-LHC S2	0.0201 %	0.0175 %
+ ILC 500 direct-top	0.0189 %	0.0175 %

Table 9. Global-fit constraints on the oblique parameters, αS and αT in Eq. (D.8). They are defined at $Q_{\text{proc}} = m_Z$, hence top-quark effects are evaluated at $Q = \max(m_t, m_Z) = m_t$. Any choice of Q_0 yields the same results.

with the energy scale. Given the covariance matrix from a global fit, one can calculate the error of the observable \mathcal{O} contributed from EFT operators as

$$\begin{aligned}
\sigma_{\mathcal{O}}^2 &= \langle \delta \mathcal{O}^2 \rangle = \sum_{I,J} a_I(Q) \mathcal{Cov}_{IJ}(Q) a_J(Q) \\
&= \sum_{I,J,K,L} a_I(Q) \Gamma_{IK}(Q/Q_0) \mathcal{Cov}_{KL}(Q_0) \Gamma_{JL}(Q/Q_0) a_J(Q) \\
&= \sum_{I,J} a_I(Q_0) \mathcal{Cov}_{IJ}(Q_0) a_J(Q_0).
\end{aligned}
\tag{D.6}$$

The second line follows from the matrix relation in Eq. (D.3). This proves that the error of a physical observable contributed from EFT coefficients is independent on our choice of Q_0 .

D.3 The interpretation of the Q_0 dependence - Oblique parameters

We turn to discuss one interesting Q_0 dependence, which provides another example of how to think of Q_0 . Figure 12 shows that the constraint on c_T varies significantly with Q_0 , because c_T receives a large anomalous dimension from top operators. As a result, its constraint is much weaker at higher Q_0 scales. Since c_T is closely related to the T parameter that signals the breaking of the custodial symmetry, does this mean that the custodial symmetry can be broken seriously at high energy? Not necessarily.

We detail these by explicitly checking that our global fit successfully impose the small breaking of the custodial symmetry at low energy $\sim m_Z$ (irrespective of Q_0) even though we do not directly use small T as an input data. The expressions of oblique parameters can be read from the expressions of well-measured electroweak precision

observables, Z -pole s_* and m_W^2/m_Z^2 , [1]

$$m_W^2/m_Z^2 = c_0^2 + \frac{c_0^2}{c_0^2 - s_0^2} (c_0^2 c_T - 2s_0^2(c'_{HL} + 8c_{WB})),$$

$$s_*^2 = s_0^2 + \frac{s_0^2}{c_0^2 - s_0^2} (c'_{HL} + 8c_{WB} - c_0^2 c_T) - \frac{1}{2}c_{HE} - s_0^2(c_{HL} - c_{HE}), \quad (\text{D.7})$$

as (generalized from [1])

$$\alpha S = 4s_0^2 (8c_{WB} + c'_{HL}) + 4 \left(-\frac{1}{2} + s_0^2 \right) c_{HE} - 4s_0^2 c_{HL},$$

$$\alpha T = c_T - \frac{c_0^2 - s_0^2}{c_0^2} c_{HE} - 2 \frac{s_0^2}{c_0^2} c_{HL}. \quad (\text{D.8})$$

These are Z -pole observables, hence defined at $Q_{\text{proc}} = m_Z$. The expressions are consistent with the oblique parameters, \hat{S} and \hat{T} , defined in the universal limit [31]

$$\hat{S} \equiv \frac{\alpha}{4s_0^2} S = g^2 \left(\frac{1}{gg'} C_{HWB} + \frac{1}{4} C_{HJW} + \frac{1}{4} C_{HJB} \right), \quad (\text{D.9})$$

$$\hat{T} \equiv \alpha T = -\frac{1}{2} C_{HD} + \frac{g'^2}{2} C_{HJB}, \quad (\text{D.10})$$

because our operators correspond to the bosonic currents in the universal theory

$$c'_{HL} \rightarrow \frac{g^2}{4} C_{HJW}, \quad c_{HL} \rightarrow \frac{g'^2}{2} Y_l C_{HJB}, \quad c_{HE} \rightarrow \frac{g'^2}{2} Y_e C_{HJB}, \quad (\text{D.11})$$

where $Y_{l,e}$ are the hypercharges of the L and e , respectively.

Using these, we numerically evaluate the global-fit constraints on αS and αT in [Table 9](#). Whether top operators are added or not, they are indeed constrained to be small for all benchmark scenarios. Top-quark effects on oblique parameters are particularly small once direct-top constraints are included. The oblique parameters are defined at $Q_{\text{proc}} = m_Z$, while top-quark effects are decoupled below m_t so that $Q = \max(m_t, m_Z) = m_t$ is used. Thus, (we checked that) these results remain true and same for any value of Q_0 , again because the constraints on physical observables are independent on Q_0 . The Q_0 -independence implies that the custodial symmetry is well preserved at low energy regardless of c_T constraints at high Q_0 .

What about the custodial symmetry at high energy scales (where c_T is weakly constrained)? First of all, c_T (at high Q_0) does not necessarily correspond to the T parameter. Eq. (D.8) shows that there can be other contributions to EW precision observables because our operator set is not assumed to be oblique or universal. At high energy scales, the meaning of T becomes more subtle too. One main reason is

that the S, T, U description is valid at low energy, as this is the Taylor expansion of self-energy corrections in powers of energy scale [29]. Also, the RG evolution itself generates the non-universal effects which cannot be absorbed into the parameters of universal theories [57]. It is expected that the non-universal effects interfere with the universal ones, making the meaning of T ambiguous. Therefore, the poor constraint on c_T at high Q_0 does not necessarily mean the large breaking of the custodial symmetry at those high scales, nor at low scales.

E RG evolution with bottom operators and their impact

Our main discussion focuses on the Higgs and top operators. But many new physics models accompany bottom operators together with top operators. The following 3 ‘bottom’ operators are relevant to us (in addition to the bottom Yukawa operator \mathcal{O}_{bH} that is already added)

$$\begin{aligned}\mathcal{O}_{Hb} &= (\Phi^\dagger_i \overleftrightarrow{D}_\mu \Phi)(\bar{b}\gamma^\mu b), \\ \mathcal{O}_{bW} &= (\bar{Q}\tau^a \sigma^{\mu\nu} b)\Phi W_{\mu\nu}^a, \\ \mathcal{O}_{bB} &= (\bar{Q}\sigma^{\mu\nu} b)\Phi B_{\mu\nu},\end{aligned}\tag{E.1}$$

with the Lagrangian

$$\Delta\mathcal{L}_{\text{bottom}} = \frac{c_{Hb}}{v^2} \mathcal{O}_{Hb} + \frac{c_{bW}}{v^2} \mathcal{O}_{bW} + \frac{c_{bB}}{v^2} \mathcal{O}_{bB}.\tag{E.2}$$

These operators are relevant in direct-top and -bottom observables at tree-level as well as Higgs + EW observables at one-loop. The tree-level effects on direct-top constraints are already taken into account in [15], from which we take our direct-top constraints.

The RG equations of dimension-6 operators are given in [39, 41–43]. Their Warsaw-basis operators can be converted to ours following the rule

$$\begin{aligned}c_H &= -2c_{H\Box} + \frac{1}{2}c_{HD}, & c_T &= -\frac{1}{2}c_{HD}, & -\frac{\lambda}{v^2}c_6 &= \frac{1}{v^2}c_{HH}, \\ \frac{g^2}{m_W^2}c_{WW} &= \frac{1}{v^2}c_{HW}, & \frac{g'^2}{m_W^2}c_{BB} &= \frac{1}{v^2}c_{HB}, & \frac{2gg'}{m_W^2}c_{WB} &= \frac{1}{v^2}c_{HWB}, \\ \frac{1}{v^2}c_{HL} &= \frac{1}{v^2}c_{Hl}^{(1)}, & \frac{1}{v^2}c'_{HL} &= \frac{1}{v^2}c_{Hl}^{(3)}, & \frac{1}{v^2}c_{HE} &= \frac{1}{v^2}c_{He},\end{aligned}\tag{E.3}$$

where operators on the right-hand side are the operators in [41] and on the left-hand side are ours; to avoid confusion, we use c_{HH} instead of c_H on the right-hand side. We keep only top contributions to Higgs operators. Keeping terms of order $\mathcal{O}(g, g', y_t, y_b)^2$, we already showed all the needed top-operator contributions in Section 3.5. In addition,

for completeness, we show the RG equations of c_6 and c_{bH} as well as additional bottom contributions to Higgs operators

$$\dot{c}_6 = -\frac{1}{\lambda} \left[(8\lambda y_t N_c - 8y_t^3 N_c) c_{tH} + (-16\lambda y_t^2 N_c + \frac{16}{3}\lambda g^2) c_{Hq}^{(3)} + 16\lambda y_t y_b N_c c_{Htb} \right] \quad (\text{E.4})$$

$$\begin{aligned} \dot{c}_{bH} = & y_t(2N_c - 3)c_{tH} + ((-4N_c + 6)y_t^2 - 2g_1^2 + \frac{4}{3}g_2^2 N_c + 12\lambda) c_{Hq}^{(3)} \\ & + (-2g_1^2 + 4\lambda)c_{Hq}^{(1)} + (-2y_t^3 + 3g_2^2 y_t - 4\lambda y_t)/y_b c_{Htb} + (-6g_2 y_t) c_{tW}. \end{aligned} \quad (\text{E.5})$$

The RG effect on c_{bH} does not vanish in the limit $y_b \rightarrow 0$ but is rather enhanced by y_t/y_b .

The bottom-operator RG contributions are (in addition to the top contributions in Section 3.5)

$$\dot{c}_H = 0, \quad (\text{E.6})$$

$$\dot{c}_T = -(4N_c y_b^2 + \frac{8}{3}g'^2 Y_h Y_d N_c) c_{Hb}, \quad (\text{E.7})$$

$$\dot{c}_{WW} = -\frac{1}{2}g N_c (y_b c_{bW}), \quad (\text{E.8})$$

$$\dot{c}_{BB} = -\frac{1}{t_W^2} g' N_c (y_b (Y_q + Y_d) c_{bB}), \quad (\text{E.9})$$

$$\dot{c}_{WB} = \frac{1}{8t_W} (-2g N_c y_b c_{bB} - 4g' (Y_q + Y_d) y_b N_c c_{bW}), \quad (\text{E.10})$$

$$\dot{c}_{HL} = \frac{1}{2} Y_l g'^2 (\frac{8}{3} Y_d N_c c_{Hb}), \quad (\text{E.11})$$

$$\dot{c}'_{HL} = 0, \quad (\text{E.12})$$

$$\dot{c}_{HE} = \frac{1}{2} Y_e g'^2 (\frac{8}{3} Y_d N_c c_{Hb}). \quad (\text{E.13})$$

Figure 13 compares the global-fit results with and without the bottom operators. The bottom operators are well constrained by HL-LHC data, which include direct-bottom productions from $Z \rightarrow b\bar{b}$ and single-top productions [15]. Their RG effects are also often suppressed by small y_b . After all, the impact of bottom operators are almost invisible. We can safely ignore bottom operators assuming that direct-top and bottom data can constrain them well.

F Observables in terms of operators

We collect numerical expressions of observables in terms of operator coefficients in Table 10 (Higgs operator), Table 11 (top-operators renormalized at $Q_0 = 1$ TeV), and Table 12 (SM parameters and the Higgs mass, although δm_h is already rewritten in terms of other parameters in the tables).

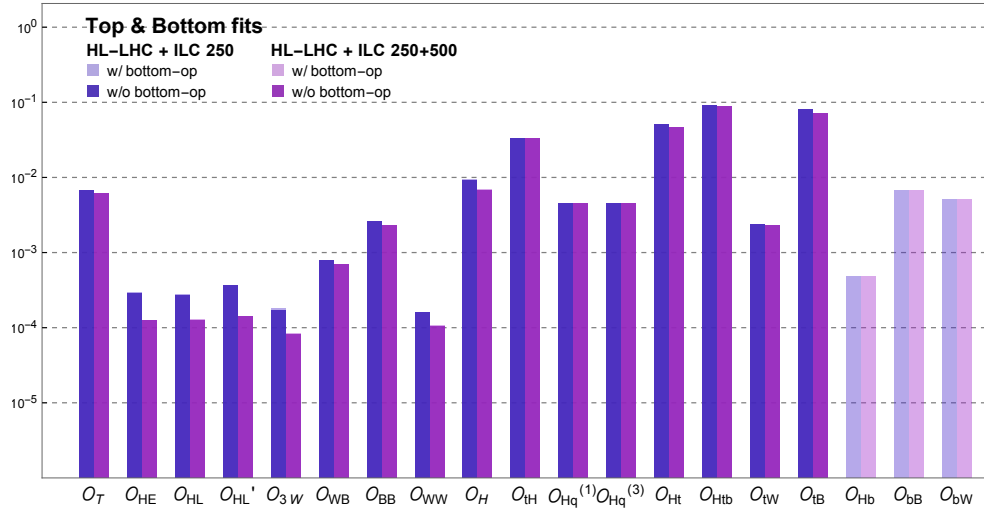


Figure 13. The global-fit 1σ constraints with (dark) and without (light) the bottom operators in Eq. (E.1) added to our work. The changes due to bottom operators are almost invisible.

Higgs Operators									
Observables	c_T	c_{HE}	c_{HL}	c'_{HL}	c_{3W}	c_{WB}	c_{BB}	c_{WW}	c_H
$\delta\alpha^{-1}$	0	0	0	0	0	3.704	-1.852	-1.852	0
δG_F	0	0	0	2.0	0	0	0	0	0
δA_l	0	14.37	12.39	12.39	0	-53.23	-22.95	76.18	0
δm_W	0	0	0	0	0	0	0	4.0	0
δm_Z	-0.5	0	0	0	0	1.852	0.279	3.074	0
δm_h	0	0	0	0	0	0	0	0	-0.5
$\delta\Gamma_l$	-0.5	-1.84	2.14	2.14	0	4.97	0.58	10.06	0
$\delta\Gamma_W$	0	0	0	0	0	0	0	12	0
$\delta\Gamma_Z$	-0.5	0	0	0	0	5.03	0.61	9.97	0
δg_{Zeff}	0	-0.651	1.301	-1.301	0	0	0	0	0
$\delta\kappa_{Aeff}$	0	1.160	1	-1	0	0	0	0	0
$\delta\lambda_{Aeff}$	0	0	0	0	-2.526	0	0	0	0
$a_L(250)$	-1.706	0	14.0	14.0	0	0.7618	-0.9244	12.71	0.0655
$a_R(250)$	-1.706	-16.23	0	0	0	8.762	2.525	1.264	0.0655
$b_L(250)$	0	0	0	0	0	0.4928	-0.827	10.74	0
$b_R(250)$	0	0	0	0	0	7.428	2.164	0.8179	0
$a_L(500)$	-1.65	0	55.99	55.99	0	0.556	-0.955	12.37	-0.412
$a_R(500)$	-1.65	-64.93	0	0	0	8.556	2.494	0.923	-0.412
$b_L(500)$	0	0	0	0	0	0.123	-0.986	11.27	0
$b_R(500)$	0	0	0	0	0	7.857	2.349	0.205	0
$\delta\sigma(\nu\bar{\nu}h, 250)$	0	0	-0.37	-4.03	0	0	0	15.84	0.85
$\delta\sigma(\nu\bar{\nu}h, 500)$	0	0	-0.19	-6.61	0	0	0	17.48	-0.4
$\delta\Gamma(h \rightarrow WW^*)$	0	0	0	0	0	0	0	-24.08	-7.8
$\delta\Gamma(h \rightarrow ZZ^*)$	2.31	0	0	0	0	-14.07	-2.293	-21.43	-8.8
$\delta\Gamma(h \rightarrow \gamma\gamma)$	0	0	0	0	0	-1963	981.6	976.4	-3.1
$\delta\Gamma(h \rightarrow Z\gamma)$	3.25	0	0	0	0	-695.8	-294.2	966.6	-5.8
$\delta\Gamma(h \rightarrow f\bar{f}) = 1 - 1.5c_H + 2c_{fH} \quad (f = b, c, \mu, \tau), \quad \delta\Gamma(h \rightarrow gg) = 1 - 1.5c_H + 2c_{gH}$									
$\delta\sigma(Zhh, L)$	-10.67	0	112.0	112.0	0	22.17	-15.14	240.4	-2.19
$\delta\sigma(Zhh, R)$	-10.67	-129.8	0	0	0	164.3	46.14	36.99	-2.19
$\delta\sigma(Zhh, U)$	-10.67	-55.34	64.27	64.27	0	82.76	10.98	153.7	-2.19

Table 10. Tree-level contributions of Higgs operators to the observables that we use. The numbers agree with [1] and are presented in absolute values not in %. They are understood as follow: for example, $\delta\alpha^{-1} = -1.852c_{WW} + 3.704c_{WB} - 1.852c_{BB} +$ (top-RG effects in Table 11) + (SM parameters in Table 12).

Top operators ($Q_0 = 1$ TeV)							
Observables	c_{tH}	$c_{HQ}^{(1)}$	$c_{HQ}^{(3)}$	c_{Ht}	c_{Htb}	c_{tW}	c_{tB}
$\delta\alpha^{-1}$	0	0	0	0	0	-0.0531	-0.0967
δG_F	0	0	-0.0187	0	0	0	0
δA_l	0	0.0386	-0.116	0.0773	0	1.3	-0.228
δm_W	0	0	0	0	0	0.043	0
δm_Z	0	-0.0668	0	0.0639	0.0016	0.0164	-0.009
δm_h	0	0	0.169	0	-0.0049	0	0
$\delta\Gamma_l$	0	-0.0682	-0.02	0.061	0.0016	0.0636	-0.0296
$\delta\Gamma_W$	0	0	0	0	0	0.129	0
$\delta\Gamma_Z$	0	-0.0668	0	0.0639	0.0016	0.0621	-0.0293
$\delta g_{Zeff}(250)$	0	0	0.0096	0	0	0	0
$\delta\kappa_{Aeff}(250)$	0	0.0025	0.0074	0.0049	0	0	0
$\delta g_{Zeff}(500)$	0	0	0.0048	0	0	0	0
$\delta\kappa_{Aeff}(500)$	0	0.0012	0.0037	0.0025	0	0	0
$a_L(250)$	0	-0.189	-0.161	0.212	0.0066	0.107	-0.0324
$a_R(250)$	0	-0.224	-0.0577	0.143	0.0066	-0.0464	-0.0053
$b_L(250)$	0	0	0	0	0	0.0877	-0.0251
$b_R(250)$	0	0	0	0	0	-0.0456	-0.0017
$a_L(500)$	0	-0.119	-0.17	0.175	0.0023	0.0635	-0.0216
$a_R(500)$	0	-0.188	0.0372	0.0373	0.0023	-0.0134	-0.008
$b_L(500)$	0	0	0	0	0	0.0474	-0.0132
$b_R(500)$	0	0	0	0	0	-0.0269	-0.0001
$\delta\sigma(\nu\bar{\nu}h, 250)$	0	-0.0003	-0.329	-0.0005	0.0104	0.156	0
$\delta\sigma(\nu\bar{\nu}h, 500)$	0	-0.0001	-0.045	-0.0001	0.002	0.156	0
$\delta\Gamma(h \rightarrow WW^*)$	0	0	2.64	0	-0.0766	-0.259	0
$\delta\Gamma(h \rightarrow ZZ^*)$	0	0.308	2.98	-0.295	-0.0939	-0.104	0.0629
$\delta\Gamma(h \rightarrow \gamma\gamma)$	-0.565*	0	1.05	0	-0.0304	28.1	51.2
$\delta\Gamma(h \rightarrow Z\gamma)$	-0.114*	0.141	2.26	-0.709	-0.0676	16.6	-2.79
$\delta\Gamma(h \rightarrow gg)$	2*	0	0.508	0	-0.0147	0	0
$\delta\Gamma(h \rightarrow f\bar{f})$	0	0	0.508	0	-0.0147	0	0
$\delta\sigma(Zhh, L)$	0	-1.06	-0.643	1.14	0.0337	1.08	-0.354
$\delta\sigma(Zhh, R)$	0	-1.20	-0.229	0.864	0.0337	-0.291	-0.114
$\delta\sigma(Zhh, U)$	0	-1.12	-0.466	1.02	0.0337	0.493	-0.251

Table 11. Contributions from top operators, written in terms of Wilson coefficients renormalized at $Q_0 = 1$ TeV. The default RG scale $Q = \max(m_t, Q_{\text{proc}})$ is used. The \mathcal{O}_{tH} contributions to $\delta\Gamma(h \rightarrow \gamma\gamma, Z\gamma, gg)$ marked with (*) are from the tree-level shift of the top Yukawa discussed in Section 3.6.

SM parameters					
Observables	δg	$\delta g'$	δv	$\delta \bar{\lambda}$	δm_h
$\delta \alpha^{-1}$	-0.463	-1.54	0	0	0
δG_F	0	0	-2.	0	0
δA_l	19.	-19.	0	0	0
δm_W	1.	0	1.	0	0
δm_Z	0.768	0.232	1.	0	0
δm_h	0	0	1.	0.5	1
$\delta \Gamma_l$	2.51	0.485	1.	0	0
$\delta \Gamma_W$	3.	0	1.	0	0
$\delta \Gamma_Z$	2.68	0.318	1.	0	0
δg_{Zeff}	0	0	0	0	0
$\delta \kappa_{Aeff}$	0	0	0	0	0
$\delta \lambda_{Aeff}$	0	0	0	0	0
$a_L(250)$	3.18	-0.767	-0.720	-0.566	-1.13
$a_R(250)$	0.316	2.10	-0.72	-0.566	-1.13
$b_L(250)$	0	0	0	0	0
$b_R(250)$	0	0	0	0	0
$a_L(500)$	3.09	-0.793	0.125	-0.088	-0.175
$a_R(500)$	0.231	2.07	0.125	-0.088	-0.175
$b_L(500)$	0	0	0	0	0
$b_R(500)$	0	0	0	0	0
$\delta \sigma(\nu \bar{\nu} h, 250)$	4.40	0	-5.30	-1.85	-3.70
$\delta \sigma(\nu \bar{\nu} h, 500)$	5.15	0	-2.05	-0.60	-1.20
$\delta \Gamma(h \rightarrow WW^*)$	-4.52	0	2.96	6.80	13.6
$\delta \Gamma(h \rightarrow ZZ^*)$	-4.37	-1.89	2.98	7.80	15.6
$\delta \Gamma(h \rightarrow \gamma\gamma)$	-0.374	3.07	0.9	2.10	4.20
$\delta \Gamma(h \rightarrow Z\gamma)$	-5.61	3.11	1.10	4.80	9.60
$\delta \Gamma(h \rightarrow gg)$	0	0	1	0.5	1
$\delta \Gamma(h \rightarrow f\bar{f})$	0	0	-1	0.5	1
$\delta \sigma(Zhh, L)$	10.6	-0.257	1.56	-1.39	-3.90
$\delta \sigma(Zhh, R)$	4.87	5.47	1.56	-1.39	-3.90
$\delta \sigma(Zhh, U)$	8.16	2.18	1.56	-1.39	-3.90

Table 12. Contributions from SM parameters δg , $\delta g'$, δv , $\delta \bar{\lambda}$. And the contributions through δm_h are also shown although they are already rewritten in terms of other parameters in [Table 12](#), [11](#), and [10](#).

G Numerical results

We tabulate numerical values for the the figures in Section 5: [Table 13](#) (Higgs couplings) and [Table 14](#) (EFT coefficients).

top data	ILC 250			ILC 250 + 500			
	w/o top	w/ top		w/o top	w/ top		
	-	LHC Run 2	HL-LHC S2	-	-	HL-LHC S2	ILC 500
hbb	0.94	1.02	0.95	0.55	1.85	0.56	0.55
hcc	1.73	1.77	1.73	1.10	2.08	1.10	1.10
$h\tau\tau$	1.08	1.15	1.08	0.71	1.90	0.72	0.71
hWW	0.48	0.62	0.49	0.35	1.81	0.36	0.35
hZZ	0.48	0.62	0.49	0.35	1.70	0.35	0.35
$h\gamma\gamma$	1.08	1.15	1.09	1.00	1.97	1.00	1.00
hgg	1.54	1.59	1.54	0.90	1.98	0.90	0.90
$h\mu\mu$	3.95	3.97	3.95	3.71	4.09	3.71	3.71
$hZ\gamma$	9.04	9.11	9.07	6.37	10.40	6.62	6.37
Γ_{inv}	0.30	0.30	0.30	0.28	0.28	0.28	0.28
Γ_{other}	1.51	1.51	1.51	1.16	1.21	1.16	1.16
Γ_{tot}	2.20	2.34	2.21	1.51	3.82	1.52	1.51
δy_t	0	12.8	3.29	0	396.	3.29	3.29
$\delta \bar{\lambda}$	0.87	1.20	0.90	0.66	3.29	0.68	0.66

Table 13. The projected uncertainties of Higgs couplings in ILC 250 (Fig. 3) and 500 (Fig. 6) stages, in %. First column shows the values without top operators. Second and third columns represent the uncertainties with direct top data of LHC Run 2 and HL-LHC S2. In ILC 250+500 fits, we present the Higgs precision evaluated without top (fourth column), “indirect only” including top operators (fifth column), plus HL-LHC S2 data (sixth column) and adding ILC 500 direct-top in the last column.

top data	ILC 250			ILC 250 + 500			
	w/o top	w/ top		w/o top	w/ top		
	-	LHC Run 2	HL-LHC S2	-		HL-LHC S2	ILC 500
c_T	0.029	2.514	0.666	0.02	3.336	0.61	0.027
c_{HE}	0.024	0.066	0.029	0.007	0.035	0.012	0.007
c_{HL}	0.025	0.042	0.027	0.011	0.027	0.013	0.011
c'_{HL}	0.035	0.04	0.036	0.012	0.05	0.014	0.012
c_{3W}	0.017	0.017	0.017	0.008	0.008	0.008	0.008
c_{WB}	0.007	0.108	0.079	0.004	0.784	0.069	0.004
c_{BB}	0.016	0.355	0.262	0.011	2.457	0.228	0.011
c_{WW}	0.016	0.021	0.016	0.01	0.178	0.01	0.01
c_H	0.885	1.385	0.916	0.656	2.313	0.674	0.657
c_{tH}	0	12.779	3.288	0	396.48	3.286	3.286
$c_{Hq}^{(1)}$	0	2.866	0.448	0	20.67	0.445	0.016
$c_{Hq}^{(3)}$	0	2.149	0.448	0	9.301	0.445	0.016
c_{Ht}	0	19.778	5.069	0	19.046	4.579	0.03
c_{Htb}	0	14.34	8.963	0	692.62	8.938	5.372
c_{tW}	0	1.237	0.234	0	10.433	0.233	0.078
c_{tB}	0	10.904	8.043	0	71.313	7.044	0.041

Table 14. The global 1σ constraints on the EFT coefficients at ILC 250 (Fig. 3) and 500 (Fig. 6) stages, in %. Details are as in Table 13.

H Covariance matrices

We present the covariance matrices of the global fits for the three benchmark scenarios. The matrices are written down in the basis,

$$(\delta g, \delta g', \delta v, \delta \bar{\lambda}, c_T, c_{HE}, c_{HL}, c'_{HL}, c_{3W}, c_{WB}, c_{BB}, c_{WW}, c_H, c_{tH}, c_{Hq}^{(1)}, c_{Hq}^{(3)}, c_{Ht}, c_{Hb}, c_{Ht}, c_{Hb}, c_{HW}, c_{tB}, c_{bH}, c_{cH}, c_{gH}, c_{\tau H}, c_{\mu H}, c_{\nu H}, \delta a_{other}, \delta a_{inv}, \delta a_{other}, C_W, C_Z) \quad (\text{H.1})$$

- Covariance matrix without top operators at ILC 250

$$10^{-8} \begin{pmatrix} 17. & -4.4 & 4.3 & -90. & 2.5 & 1.1 & 3.9 & 4.3 & 0.18 & -0.067 & 5.2 & -5.4 & -81. & 3.5 & 3.9 & 3.9 & 8.2 & -45. & 0 & 6.7 & 4.4 & 1.5 \\ -4.4 & 2. & -1.2 & 19. & -1.1 & -0.35 & -1.1 & -1.2 & -0.055 & -0.14 & -1.7 & 1.4 & 17. & -1.4 & -1.4 & -1.4 & -2.6 & -7.8 & 0 & -2.3 & -1.2 & -0.22 \\ 4.3 & -1.2 & 13. & 39. & -1.3 & -4.1 & 3. & 13. & 2. & -1.8 & 0.55 & -4.3 & 64. & -17. & -18. & -18. & -5.8 & -23. & 0 & -3.2 & 13. & 13. \\ -90. & 19. & 39. & 7.6 \times 10^3 & 8.9 & 1.1 & 64. & 72. & 39. & -13. & -2.8 & -18. & 13. & 7.7 \times 10^3 & 1.1 \times 10^2 & 1.4 \times 10^2 & 1.3 \times 10^2 & -96. & 1.8 \times 10^2 & 0 & 5.0 \times 10^3 & 36. & 48. \\ 2.5 & -1.1 & -1.3 & 8.9 & 8.4 & 4.5 & 3.7 & -1.3 & -0.88 & 1.6 & 3.3 & -0.047 & 6.2 & -0.31 & -0.24 & -0.23 & -1.6 & -15. & 0 & 3.4 & -2.8 & -5.3 \\ 1.1 & -0.35 & -4.1 & -64. & 4.5 & 5.9 & 0.32 & -4.1 & -0.61 & 1.4 & 2.1 & 0.75 & -72. & 6.3 & 7.1 & 7.1 & 3. & -3.3 & 0 & 3.4 & -4.2 & -6.3 \\ 3.9 & -1.1 & 3. & 72. & 3.7 & 0.32 & 6.5 & 3. & -0.82 & 0.43 & 2.6 & -1.8 & 78. & -1.7 & -2.5 & -2.5 & 0.57 & -17. & 0 & 0.88 & 3.3 & 1.3 \\ 4.3 & -1.2 & 13. & 39. & -1.3 & -4.1 & 3. & 13. & 2. & -1.8 & 0.55 & -4.3 & 64. & -17. & -18. & -18. & -5.8 & -23. & 0 & -3.2 & 13. & 13. \\ 0.18 & -0.055 & 2. & -13. & -0.88 & -0.61 & -0.82 & 2. & 2.9 & -0.44 & -0.33 & -0.55 & -9. & -3.3 & -3.3 & -3.3 & -1.3 & -1.7 & 0 & -0.73 & 2. & 2.5 \\ -0.067 & -0.14 & -1.8 & -2.8 & 1.6 & 1.4 & 0.43 & -1.8 & -0.44 & 0.55 & 0.61 & 0.5 & -6.4 & 2.4 & 2.6 & 2.6 & 0.76 & -0.031 & 0 & 1.1 & -2. & -2.6 \\ 5.2 & -1.7 & 0.55 & -18. & 3.3 & 2.1 & 2.6 & 0.55 & -0.33 & 0.61 & 2.6 & -1.4 & -17. & 2.3 & 2.4 & 2.4 & 3. & 1.2 & 0 & 3.1 & 0.46 & -1.4 \\ -5.4 & 1.4 & -4.3 & 13. & -0.047 & 0.75 & -1.8 & -4.3 & -0.55 & 0.5 & -1.4 & 2.4 & 4.7 & 3.1 & 3.3 & 3.3 & -0.97 & 17. & 0 & -0.84 & -4.5 & -3.9 \\ -81. & 17. & 64. & 7.7 \times 10^3 & 6.2 & -72. & 78. & 64. & -9. & -6.4 & -17. & 4.7 & 7.8 \times 10^3 & 1.7 \times 10^2 & 1.9 \times 10^2 & 1.9 \times 10^2 & 1.3 \times 10^2 & 1.1 \times 10^2 & 0 & 5.0 \times 10^3 & 62. & 74. \\ 3.5 & -1.4 & -17. & 1.1 \times 10^3 & -0.31 & 6.3 & -1.7 & -17. & -3.3 & 2.4 & 2.3 & 3.1 & 1.7 \times 10^2 & 6.8 \times 10^3 & 6.2 \times 10^3 & 6.2 \times 10^3 & 6.2 \times 10^3 & 8.1 \times 10^2 & 0 & 2.3 \times 10^3 & -2. & -17. \\ 3.9 & -1.4 & -18. & 1.4 \times 10^2 & -0.24 & 7.1 & -2.5 & -18. & -3.3 & 2.6 & 2.4 & 3.3 & 1.9 \times 10^2 & 6.2 \times 10^3 & 2.8 \times 10^4 & 6.2 \times 10^3 & 6.2 \times 10^3 & 8.1 \times 10^2 & 0 & 1.7 \times 10^3 & -3.3 & -18. \\ 3.9 & -1.4 & -18. & 1.3 \times 10^2 & -0.23 & 7.1 & -2.5 & -18. & -3.3 & 2.6 & 2.4 & 3.3 & 1.9 \times 10^2 & 6.2 \times 10^3 & 2.2 \times 10^4 & 6.2 \times 10^3 & 6.2 \times 10^3 & 8.1 \times 10^2 & 0 & 3.5 \times 10^4 & -3.3 & -18. \\ 8.2 & -2.6 & -5.8 & -96. & -1.6 & 3. & 0.57 & -5.8 & -1.3 & 0.76 & 3. & -0.97 & 1.3 \times 10^2 & 6.2 \times 10^3 & 6.2 \times 10^3 & 6.2 \times 10^3 & 9.4 \times 10^3 & 7.8 \times 10^2 & 0 & 2.6 \times 10^3 & 9.5 & -5. \\ -45. & -7.8 & -23. & 1.8 \times 10^2 & -15. & -3.3 & -17. & -23. & -1.7 & -0.031 & 1.2 & 17. & 1.1 \times 10^2 & 8.1 \times 10^2 & 8.1 \times 10^2 & 8.1 \times 10^2 & 7.8 \times 10^2 & 1.5 \times 10^5 & 0 & 2.5 \times 10^2 & -21. & -2.2 \\ 0 & 0 & 0 & 0 & 0 & 0 & 0 & 0 & 0 & 0 & 0 & 0 & 0 & 0 & 0 & 0 & 0 & 0 & 3.3 \times 10^2 & 3.3 \times 10^2 & 0 & 0 \\ 6.7 & -2.3 & -3.2 & 5.0 \times 10^3 & 3.4 & 3.4 & 0.88 & -3.2 & -0.73 & 1.1 & 3.1 & -0.84 & 5.0 \times 10^3 & 2.3 \times 10^3 & 1.7 \times 10^3 & 3.5 \times 10^2 & 2.6 \times 10^3 & 2.5 \times 10^2 & 3.3 \times 10^2 & 8.0 \times 10^3 & -3.1 & -5.9 \\ 4.4 & -1.2 & 13. & 36. & -2.8 & -4.2 & 3.3 & 13. & 2. & -2. & 0.46 & -4.5 & 62. & -2. & -3.3 & -3.3 & 9.5 & -21. & 0 & -3.1 & 37. & 14. \\ 1.5 & -0.22 & 13. & 48. & -5.3 & -6.3 & 1.3 & 13. & 2.5 & -2.6 & -1.4 & -3.9 & 74. & -17. & -18. & -18. & -5. & -2.2 & 0 & -5.9 & 14. & 38. \end{pmatrix} \quad (\text{H.2})$$

• Covariance matrix for LHC run 2 + ILC 250

$$\begin{pmatrix}
 0.8 & -0.67 & 0.33 & 10. & -64. & 17. & 1.1 & 0.47 & 0.014 & 1.3 & -4.4 & -0.66 & 16. & 1.2 \times 10^2 & -21. & 15. & 5.2 \times 10^2 & -0.69 & -10. & 1.5 \times 10^2 & 1.4 & 1.3 & 1.2 \times 10^2 & 1.7 & -3.6 & 0 & 0.36 & 0.24 & 0.1 \\
 -0.67 & 0.33 & -0.078 & -4.7 & 10. & -0.51 & -0.32 & -0.12 & -0.004 & -0.4 & 1.3 & 0.15 & -6.4 & 77. & 5.6 & -4.5 & 1.8 \times 10^2 & -0.35 & 3.1 & 4.5 & -0.43 & -0.30 & 77. & -0.46 & -1 & 0 & -0.46 & -0.08 & -0.0016 \\
 0.33 & -0.078 & 1.3 & 4.9 & -3.5 & -0.39 & 3.4 & 1.3 & 0.21 & -0.9 & 2.6 & -0.48 & 5.4 & -14. & 0.0055 & -6.5 & -27 & 0.11 & 5.3 & -78. & -1.9 & -2.1 & 12 & -0.71 & -2.4 & 0 & -0.41 & 1.4 & 4.4 & 7.6 \\
 10. & -4.7 & 4.9 & 1.4 \times 10^2 & 2.0 \times 10^3 & 40. & 3.1 & 3.8 & 1.3 & 0.21 &td>
 \end{pmatrix}$$

(H.3)

• Covariance matrix for HL-LHC S2 + ILC 250

$$\begin{pmatrix}
 10. & -4.8 & 3.8 & -72 & 37. & 1.9 & 3.9 & 0.16 & 7.6 & -20. & -5.6 & -64. & 73. & 0.43 & -0.43 & 3.0 \times 10^2 & -0.7 & -3.9 & 7.0 \times 10^2 & 5.5 & 5.8 & 78. & 9.6 & -4.4 & 0 & 7. & 3.9 & 1. & -0.066 \\
 -4.8 & 3.8 & -1.3 & 38. & -6.6 & -3.9 &td>
 \end{pmatrix}$$

(H.4)

• Covariance matrix for ILC 250+500 + HL-LHC S2

$$\begin{pmatrix}
 1.4 & -0.35 & 0.054 & -0.15 & -2.5 & 0.090 & 0.11 & 0.050 & -0.039 & 0.89 & -9.7 & -0.35 & -4.1 & -0.47 & 0.47 & -20 & -10 & -0.46 & 0.2 & 0.82 & 1.3 & 6.1 & 2 & -2 & 0 & 2.9 & 0.047 & -0.13 \\
 -0.35 & 0.18 & -0.042 & 0.89 & -1.5 & 0.090 & -0.027 & -0.033 & 0.0038 & -0.29 & 0.78 & 0.90 & 0.8 & -5.7 & 0.14 & -0.14 & 5.1 & 2.2 & 0.16 & -28 & -0.27 & -0.26 & 5.4 & -0.19 & -1 & 0 & -0.71 & -0.032 & 0.58 \\
 0.054 & -0.042 & 0.19 & -1.7 & 1.8 & -0.038 & -0.022 & 0.18 & 0.038 & -0.11 & 1.3 & -0.062 & -1.5 & -0.64 & 0.48 & -0.48 & 1.4 & 0.81 & 0.12 & -40 & -0.27 & -0.27 & 5.4 & -0.19 & -0.14 & 0 & -0.41 & 0.19 & 0.19 \\
 -1.5 & 0.89 & -0.17 & 4.6 \times 10^2 & -89 & 0.49 & 1.2 & -2 & -0.54 & -0.2 & -0.37 & 2.7 & 0.23 & -0.3 & 38 & -38 & 6.6 \times 10^2 & 2.2 \times 10^2 & 2.6 & -31 & 0.34 & -4.9 & -38 & -23 & 11 & 0 & 3.8 \times 10^2 & -2.1 & -1.2 \\
 -2.5 & 0.59 & 1.8 & -89 & 3.7 \times 10^2 & -6 & -0.56 & 2.5 & -0.023 & 0.76 & 2.7 & 0.23 & -0.3 & 38 & -38 & 6.6 \times 10^2 & 2.2 \times 10^2 & 2.6 & -31 & 0.34 & -4.9 & -38 & -23 & 11 & 0 & 3.8 \times 10^2 & -2.1 & -1.2 \\
 0.090 & -0.037 & -0.038 & 0.89 & -6 & 0.15 & 0.042 & -0.066 & -0.043 & 0.04 & 0.15 & -0.044 & -0.12 & -0.72 & 0.86 & -0.86 & -0.8 & 0.24 & -4.2 & 0.13 & 0.005 & 0.86 & -0.064 & -0.4 & 0 & 0.086 & -0.044 & -0.044 \\
 0.11 & -0.027 & -0.022 & 1.2 & -0.56 & 0.042 & -0.066 & -0.043 & 0.04 & 0.15 & -0.044 & -0.12 & -0.72 & 0.86 & -0.86 & -0.8 & 0.24 & -4.2 & 0.13 & 0.005 & 0.86 & -0.064 & -0.4 & 0 & 0 & 0.086 & -0.044 & -0.044 \\
 -0.039 & 0.0038 & 0.038 & -0.54 & -0.223 & -0.043 & 0.034 & 0.038 & 0.067 & -0.0089 & -0.11 & -0.084 & -0.41 & -0.089 & 4.8 & -0.16 & 0.15 & 0.17 & -0.039 & -0.011 & 0.0339 & 0.023 & -0.07 & -0.065 & -0.11 & -0.02 & -0.01 & -0.014 & 0.037 & 0.049 & 0.89 \\
 0.89 & -0.29 & -0.41 & -0.2 & 2.5 & 0.046 & -0.02 & 0.2 & 0.038 & -0.41 & 1.3 & -0.062 & -1.2 & -0.72 & 0.86 & -0.86 & -0.8 & 0.24 & -4.2 & 0.13 & 0.005 & 0.86 & -0.064 & -0.4 & 0 & 0 & -0.42 & 0.18 & 0.18 \\
 -0.29 & 0.78 & 1.3 & -0.37 & 2.7 & 0.15 & 1.4 & 1.3 & -0.011 & -0.16 & 5.2 & 0.34 & 2.3 & -3.8 & -1.4 & -0.03 &td>
 \end{pmatrix}$$

(H.7)

• Covariance matrix for ILC 250+500 + HL-LHC S2 + ILC 500-top

$$\begin{pmatrix}
 17 & -4.4 & 4.3 & -0.1 & 2.5 & 1.1 & 3.9 & 4.3 & 0.18 & -0.089 & 5.1 & -5.4 & -8.2 & -7.8 & -0.003 & 0.003 & -0.18 & -0.11 & -0.32 & 0.26 & 3.6 & 3.9 & 8.2 & 8.2 & -4.5 & 0 & 6.7 & 4.4 & 1.5 \\
 -4.4 & 2 & -1.2 & 13 &td>
 \end{pmatrix}$$

(H.8)

References

- [1] T. Barklow, K. Fujii, S. Jung, M. E. Peskin and J. Tian, *Model-Independent Determination of the Triple Higgs Coupling at $e+e-$ Colliders*, *Phys. Rev.* **D97** (2018) 053004 [[1708.09079](#)].
- [2] G. Durieux, J. Gu, E. Vryonidou and C. Zhang, *Probing top-quark couplings indirectly at Higgs factories*, *Chin. Phys.* **C42** (2018) 123107 [[1809.03520](#)].
- [3] E. Vryonidou and C. Zhang, *Dimension-six electroweak top-loop effects in Higgs production and decay*, *JHEP* **08** (2018) 036 [[1804.09766](#)].
- [4] CLICDP, CLIC collaboration, *The Compact Linear Collider (CLIC) - 2018 Summary Report*, *CERN Yellow Rep. Monogr.* **1802** (2018) 1 [[1812.06018](#)].
- [5] L. Linssen, A. Miyamoto, M. Stanitzki and H. Weerts, *Physics and Detectors at CLIC: CLIC Conceptual Design Report*, [1202.5940](#).
- [6] FCC collaboration, *FCC-ee: The Lepton Collider*, *Eur. Phys. J. ST* **228** (2019) 261.
- [7] CEPC STUDY GROUP collaboration, *CEPC Conceptual Design Report: Volume 2 - Physics & Detector*, [1811.10545](#).
- [8] P. Bambade et al., *The International Linear Collider: A Global Project*, [1903.01629](#).
- [9] H. Baer, T. Barklow, K. Fujii, Y. Gao, A. Hoang, S. Kanemura et al., *The International Linear Collider Technical Design Report - Volume 2: Physics*, [1306.6352](#).
- [10] ATLAS, CMS collaboration, *Measurements of the Higgs boson production and decay rates and constraints on its couplings from a combined ATLAS and CMS analysis of the LHC pp collision data at $\sqrt{s} = 7$ and 8 TeV*, *JHEP* **08** (2016) 045 [[1606.02266](#)].
- [11] J. Ellis, C. W. Murphy, V. Sanz and T. You, *Updated Global SMEFT Fit to Higgs, Diboson and Electroweak Data*, *JHEP* **06** (2018) 146 [[1803.03252](#)].
- [12] I. Brivio, J. Gonzalez-Fraile, M. C. Gonzalez-Garcia and L. Merlo, *The complete HEFT Lagrangian after the LHC Run I*, *Eur. Phys. J.* **C76** (2016) 416 [[1604.06801](#)].
- [13] I. Brivio, S. Bruggisser, F. Maltoni, R. Moutafis, T. Plehn, E. Vryonidou et al., *O new physics, where art thou? A global search in the top sector*, *JHEP* **02** (2020) 131 [[1910.03606](#)].
- [14] N. P. Hartland, F. Maltoni, E. R. Nocera, J. Rojo, E. Slade, E. Vryonidou et al., *A Monte Carlo global analysis of the Standard Model Effective Field Theory: the top quark sector*, *JHEP* **04** (2019) 100 [[1901.05965](#)].
- [15] G. Durieux, A. Irlles, V. Miralles, A. Peuelas, R. Pschl, M. Perell et al., *The electro-weak couplings of the top and bottom quarks – global fit and future prospects*, *JHEP* **12** (2019) 098 [[1907.10619](#)].

- [16] A. Buckley, C. Englert, J. Ferrando, D. J. Miller, L. Moore, M. Russell et al., *Constraining top quark effective theory in the LHC Run II era*, *JHEP* **04** (2016) 015 [[1512.03360](#)].
- [17] A. Buckley, C. Englert, J. Ferrando, D. J. Miller, L. Moore, M. Russell et al., *Global fit of top quark effective theory to data*, *Phys. Rev.* **D92** (2015) 091501 [[1506.08845](#)].
- [18] S. Banerjee, R. S. Gupta, J. Y. Reiness, S. Seth and M. Spannowsky, *Towards the ultimate differential SMEFT analysis*, [1912.07628](#).
- [19] T. Barklow, K. Fujii, S. Jung, R. Karl, J. List, T. Ogawa et al., *Improved Formalism for Precision Higgs Coupling Fits*, *Phys. Rev.* **D97** (2018) 053003 [[1708.08912](#)].
- [20] G. Durieux, M. Perell, M. Vos and C. Zhang, *Global and optimal probes for the top-quark effective field theory at future lepton colliders*, *JHEP* **10** (2018) 168 [[1807.02121](#)].
- [21] M. Awramik, M. Czakon, A. Freitas and G. Weiglein, *Precise prediction for the W boson mass in the standard model*, *Phys. Rev. D* **69** (2004) 053006 [[hep-ph/0311148](#)].
- [22] S. Dawson et al., *Working Group Report: Higgs Boson*, in *Community Summer Study 2013: Snowmass on the Mississippi (CSS2013) Minneapolis, MN, USA, July 29-August 6, 2013*, 2013, [1310.8361](#), <http://inspirehep.net/record/1262795/files/arXiv:1310.8361.pdf>.
- [23] K. Agashe, R. Contino and A. Pomarol, *The Minimal composite Higgs model*, *Nucl. Phys.* **B719** (2005) 165 [[hep-ph/0412089](#)].
- [24] D. B. Kaplan and H. Georgi, *$SU(2) \times U(1)$ Breaking by Vacuum Misalignment*, *Phys. Lett.* **136B** (1984) 183.
- [25] K. Agashe, R. Contino, L. Da Rold and A. Pomarol, *A Custodial symmetry for $Zb\bar{b}$* , *Phys. Lett.* **B641** (2006) 62 [[hep-ph/0605341](#)].
- [26] C. Grojean, O. Matsedonskyi and G. Panico, *Light top partners and precision physics*, *JHEP* **10** (2013) 160 [[1306.4655](#)].
- [27] F. Richard, *Present and future constraints on top EW couplings*, [1403.2893](#).
- [28] G. Durieux and O. Matsedonskyi, *The top-quark window on compositeness at future lepton colliders*, *JHEP* **01** (2019) 072 [[1807.10273](#)].
- [29] M. E. Peskin and T. Takeuchi, *A New constraint on a strongly interacting Higgs sector*, *Phys. Rev. Lett.* **65** (1990) 964.
- [30] M. E. Peskin and T. Takeuchi, *Estimation of oblique electroweak corrections*, *Phys. Rev.* **D46** (1992) 381.
- [31] J. D. Wells and Z. Zhang, *Effective theories of universal theories*, *JHEP* **01** (2016) 123 [[1510.08462](#)].

- [32] J. De Blas, G. Durieux, C. Grojean, J. Gu and A. Paul, *On the future of Higgs, electroweak and diboson measurements at lepton colliders*, *JHEP* **12** (2019) 117 [[1907.04311](#)].
- [33] S. Di Vita, G. Durieux, C. Grojean, J. Gu, Z. Liu, G. Panico et al., *A global view on the Higgs self-coupling at lepton colliders*, *JHEP* **02** (2018) 178 [[1711.03978](#)].
- [34] M. McCullough, *An Indirect Model-Dependent Probe of the Higgs Self-Coupling*, *Phys. Rev.* **D90** (2014) 015001 [[1312.3322](#)].
- [35] S. Di Vita, C. Grojean, G. Panico, M. Riemann and T. Vantalon, *A global view on the Higgs self-coupling*, *JHEP* **09** (2017) 069 [[1704.01953](#)].
- [36] LCC PHYSICS WORKING GROUP collaboration, *Tests of the Standard Model at the International Linear Collider*, [1908.11299](#).
- [37] S. Boselli, R. Hunter and A. Mitov, *Prospects for the determination of the top-quark Yukawa coupling at future e^+e^- colliders*, *J. Phys.* **G46** (2019) 095005 [[1805.12027](#)].
- [38] C. Zhang, N. Greiner and S. Willenbrock, *Constraints on Non-standard Top Quark Couplings*, *Phys. Rev.* **D86** (2012) 014024 [[1201.6670](#)].
- [39] C. Grojean, E. E. Jenkins, A. V. Manohar and M. Trott, *Renormalization Group Scaling of Higgs Operators and $\Gamma(h \rightarrow \gamma\gamma)$* , *JHEP* **04** (2013) 016 [[1301.2588](#)].
- [40] S. Jung, P. Ko, Y. W. Yoon and C. Yu, *Renormalization group-induced phenomena of top pairs from four-quark effective operators*, *JHEP* **08** (2014) 120 [[1406.4570](#)].
- [41] R. Alonso, E. E. Jenkins, A. V. Manohar and M. Trott, *Renormalization Group Evolution of the Standard Model Dimension Six Operators III: Gauge Coupling Dependence and Phenomenology*, *JHEP* **04** (2014) 159 [[1312.2014](#)].
- [42] E. E. Jenkins, A. V. Manohar and M. Trott, *Renormalization Group Evolution of the Standard Model Dimension Six Operators I: Formalism and λ Dependence*, *JHEP* **10** (2013) 087 [[1308.2627](#)].
- [43] E. E. Jenkins, A. V. Manohar and M. Trott, *Renormalization Group Evolution of the Standard Model Dimension Six Operators II: Yukawa Dependence*, *JHEP* **01** (2014) 035 [[1310.4838](#)].
- [44] S. Weinberg, *Effective Gauge Theories*, *Phys. Lett. B* **91** (1980) 51.
- [45] ALEPH, CDF, D0, DELPHI, L3, OPAL, SLD, LEP ELECTROWEAK WORKING GROUP, TEVATRON ELECTROWEAK WORKING GROUP, SLD ELECTROWEAK AND HEAVY FLAVOUR GROUPS collaboration, *Precision Electroweak Measurements and Constraints on the Standard Model*, [1012.2367](#).
- [46] *Projections for measurements of Higgs boson signal strengths and coupling parameters*

with the ATLAS detector at a HL-LHC, Tech. Rep. ATL-PHYS-PUB-2014-016, CERN, Geneva, Oct, 2014.

- [47] PHYSICS OF THE HL-LHC WORKING GROUP collaboration, *Higgs Physics at the HL-LHC and HE-LHC*, [1902.00134](#).
- [48] G. P. Lepage, P. B. Mackenzie and M. E. Peskin, *Expected Precision of Higgs Boson Partial Widths within the Standard Model*, [1404.0319](#).
- [49] M. S. Amjad et al., *A precise characterisation of the top quark electro-weak vertices at the ILC*, *Eur. Phys. J.* **C75** (2015) 512 [[1505.06020](#)].
- [50] J. Alison et al., *Higgs Boson Pair Production at Colliders: Status and Perspectives*, in *Double Higgs Production at Colliders Batavia, IL, USA, September 4, 2018-9, 2019*, B. Di Micco, M. Gouzevitch, J. Mazzitelli and C. Vernieri, eds., 2019, [1910.00012](#), <https://lss.fnal.gov/archive/2019/conf/fermilab-conf-19-468-e-t.pdf>.
- [51] J. de Blas et al., *Higgs Boson Studies at Future Particle Colliders*, *JHEP* **01** (2020) 139 [[1905.03764](#)].
- [52] A. Azatov, R. Contino, G. Panico and M. Son, *Effective field theory analysis of double Higgs boson production via gluon fusion*, *Phys. Rev.* **D92** (2015) 035001 [[1502.00539](#)].
- [53] C. F. Durig, *Measuring the Higgs Self-coupling at the International Linear Collider*, Ph.D. thesis, Hamburg U., Hamburg, 2016.
- [54] A. Azatov, C. Grojean, A. Paul and E. Salvioni, *Resolving gluon fusion loops at current and future hadron colliders*, *JHEP* **09** (2016) 123 [[1608.00977](#)].
- [55] M. L. Mangano, T. Plehn, P. Reimitz, T. Schell and H.-S. Shao, *Measuring the Top Yukawa Coupling at 100 TeV*, *J. Phys. G* **43** (2016) 035001 [[1507.08169](#)].
- [56] M. Peskin and J. Tian, *The Higgs self-coupling*, [in preparation](#).
- [57] J. D. Wells and Z. Zhang, *Renormalization group evolution of the universal theories EFT*, *JHEP* **06** (2016) 122 [[1512.03056](#)].